



# Thermal models of dyke intrusion during development of continent–ocean transition

Katherine A. Daniels, I. D. Bastow, D. Keir, R.S.J. Sparks, Thierry Menand

## ► To cite this version:

Katherine A. Daniels, I. D. Bastow, D. Keir, R.S.J. Sparks, Thierry Menand. Thermal models of dyke intrusion during development of continent–ocean transition. *Earth and Planetary Science Letters*, Elsevier, 2014, 385, pp.145-153. <10.1016/j.epsl.2013.09.018>. <hal-01131788>

**HAL Id: hal-01131788**

**<https://hal.archives-ouvertes.fr/hal-01131788>**

Submitted on 17 Mar 2015

**HAL** is a multi-disciplinary open access archive for the deposit and dissemination of scientific research documents, whether they are published or not. The documents may come from teaching and research institutions in France or abroad, or from public or private research centers.

L'archive ouverte pluridisciplinaire **HAL**, est destinée au dépôt et à la diffusion de documents scientifiques de niveau recherche, publiés ou non, émanant des établissements d'enseignement et de recherche français ou étrangers, des laboratoires publics ou privés.

1 Thermal models of dyke intrusion during development of Continent-  
2 Ocean Transition

3 Daniels, K.A.<sup>1\*</sup>, Bastow, I.D.<sup>2</sup>, Keir, D.<sup>3</sup>, Sparks, R.S.J.<sup>1</sup> and Menand, T.<sup>4,5,6</sup>

4 <sup>1</sup>School of Earth Sciences, University of Bristol, Wills Memorial Building, Queen's Road,  
5 Bristol, BS8 1RJ, U.K.

6 <sup>2</sup>Department of Earth Science and Engineering, Imperial College London, Exhibition Road,  
7 London, SW7 2AZ, U.K.

8 <sup>3</sup>National Oceanography Centre Southampton, University of Southampton, European Way,  
9 Southampton, SO14 3ZH, U.K.

10 <sup>4</sup>Clermont Université, Université Blaise Pascal, Laboratoire Magmas et Volcans, BP 10448,  
11 F-63000, Clermont-Ferrand, France.

12 <sup>5</sup>CNRS, UMR 6524, LMV, F-63038 Clermont-Ferrand, France.

13 <sup>6</sup>IRD, R 163, LMV, F-63038 Clermont-Ferrand, France.

14 \*Present address: Department of Earth Sciences, University of Cambridge, Downing Street,  
15 Cambridge, CB2 3EQ, U.K.

16

17 Email addresses: kad43@cam.ac.uk; I.Bastow@imperial.ac.uk; D.Keir@soton.ac.uk;

18 Steve.Sparks@bristol.ac.uk; T.Menand@opgc.univ-bpclermont.fr;

19 Keywords: Dyke intrusion; Magmatic extension; Continental rifting; Heat-flow; Thermal  
20 modelling.

21

22 **Abstract**

23 A consensus has emerged in recent years from a variety of geoscientific disciplines that  
24 extension during continental rifting is achieved only partly by plate stretching: dyke intrusion  
25 also plays an important role. Magma intrusion can accommodate extension at lower yield

26 stresses than are required to extend thick, strong, unmodified continental lithosphere  
27 mechanically, thereby aiding the breakup process. Dyke intrusion is also expected to heat  
28 and thereby weaken the plate, but the spatial extent of heating and the effect of different  
29 rates of magmatic extension on the timescales over which heating occurs are poorly  
30 understood. To address this issue, a numerical solution to the heat flow equation is  
31 developed here to quantify the thermal effects of dyke intrusion on the continental crust  
32 during rifting. The thermal models are benchmarked against a priori constraints on crustal  
33 structure and dyke intrusion episodes in Ethiopia. Finite difference models demonstrate that  
34 magmatic extension rate exerts a first order control on the crustal thermal structure. Once  
35 dyke intrusion supersedes faulting and stretching as the principal extensional mechanism  
36 the crust will heat and weaken rapidly (less than 1 Ma).

37 In the Main Ethiopian Rift (MER), the majority of present-day extension is focused on ~20  
38 km-wide Quaternary-Recent axial magmatic segments that are mostly seismogenic to mid-  
39 crustal depths and show P-wave seismic velocities characteristic of heavily intruded  
40 continental crust. When reviewed in light of our models, these observations require that no  
41 more than half of the MER's extension since ~2Ma has been achieved by dyke intrusion.  
42 Magmatic heating and weakening of the crust would have rendered it aseismic if dyke  
43 intrusion accounted for the entire 6 mm/yr extension rate. In the older, faster extending (16  
44 mm/yr) Red Sea rift (RSR) in Afar, dyke intrusion is expected to have had a more dramatic  
45 impact on crustal rheology. Accordingly, effective elastic plate thickness and Moho depth in  
46 the Danakil region of northernmost Afar are markedly reduced and seismicity is shallower  
47 than in the MER. Thermally driven variations in crustal rheology over time in response to  
48 dyke intrusion thus play an important role in the development of continent-ocean transition.

49

## 50 **1. Introduction**

51 It is well established that continental rifts develop initially in a mechanical fashion, with along  
52 axis segmentation governed by large-scale border faults defining early half-graben rift  
53 morphology (e.g., Hayward and Ebinger 1996). A consensus is gradually emerging from a  
54 number of tectonically active rifts and rifted continental margins worldwide, however, that  
55 magma intrusion also plays an important role in extension prior to the onset of sea-floor  
56 spreading (e.g., Maguire et al. 2006, White et al. 2008, Thybo and Nielsen 2009). This is an  
57 appealing idea, since it obviates the need for large-scale tectonic forces to rupture thick,  
58 strong cratonic lithosphere: dyke intrusion can occur at lower stresses than are required for  
59 the stretching of thick continental lithosphere (e.g., Buck 2004, 2006, Bialas et al., 2010).  
60 However, the subsequent effect of magma intrusion on the thermal structure (and by  
61 inference, the strength) of the plate over time is poorly understood. It likely has important  
62 implications for the thermal evolution and subsidence history of the extending plate (e.g.,  
63 Thybo and Nielsen 2009), including whether or not continent-ocean transition is heralded by  
64 an abrupt episode of continental plate thinning and subsidence after a period of heating and  
65 weakening by protracted magma intrusion (Bastow and Keir 2011; Keir et al., 2013).

66 To address these issues, a thermal model is developed to understand better the evolution of  
67 continental crust during extension by dyke intrusion. The model space is parameterised as  
68 an array of cells for which the heat-flow equation is solved numerically by finite difference  
69 scheme. The effects of variable magma temperature, dyke injection frequency and size, and  
70 geothermal gradient on the thermal evolution of the crust over time during rifting are tested  
71 by mapping the solidus and 600°C isotherm (representing the brittle-ductile transition  
72 temperature) positions. In a tectonically active rift this is a testable hypothesis seismically,  
73 since crustal seismicity is not expected to develop at temperatures greater than ~600°C  
74 (e.g., Maggi et al., 2000a).

75 To ground-truth the thermal models and input parameters, this study draws on geoscientific  
76 constraints from on-going extension in the East African (EAR) and Red Sea (RSR) rift  
77 systems in Ethiopia (Figure 1). The region exposes sub-aerially several sections of

78 asynchronous rift sector development above a hot (e.g., Rooney et al., 2012; Ferguson et  
79 al., 2013), low wavespeed (Bastow et al., 2008) mantle; from embryonic continental rifting in  
80 the slowly (~6 mm/yr) extending Main Ethiopian rift (MER) in the south (Kogan et al., 2012),  
81 to incipient oceanic spreading in the more rapidly extending RSR and Gulf of Aden Rift in  
82 Afar (e.g., Hayward and Ebinger, 1996; McClusky et al., 2010). Real-time geodetic and  
83 seismic observations of dyke intrusion episodes (Wright et al. 2006, Keir et al. 2009, Grandin  
84 et al., 2011) are available from the region, offering considerable advantage over studies of  
85 extinct or buried rifted margins in constraining when and how dykes intrude the crust. The  
86 region is also well-understood geophysically, with detailed constraints on parameters such  
87 as crustal thickness, effective elastic plate thickness and P-wave seismic velocity structure  
88 all available (for reviews, see e.g., Bastow et al., 2011; Keir et al., 2013).

89 In the MER, a combination of GPS surveys and structural geology studies point towards  
90 ~80% of present-day strain being accommodated at least partly by magma intrusion within a  
91 relatively narrow (~20 km) rift-axial zone, also known as the Wonji Fault Belt (WFB: Mohr  
92 1967, Ebinger and Casey 2001). However, precisely what proportion of extension has been  
93 accommodated by dyke intrusion into the still-thick MER crust since ~2 Ma is uncertain. In  
94 the Danakil depression, where crustal thickness is markedly thinner than elsewhere in Afar  
95 (Makris and Ginzburg 1987), it has been proposed that Pliocene-Recent basin development  
96 and voluminous Quaternary volcanism are the result of a late-stage of plate stretching  
97 following a protracted period of localised magma-intrusion (Bastow and Keir 2011, Keir et al.  
98 2013). This study explores whether episodes of dyke intrusion during continental breakup  
99 are capable of heating the continental crust sufficiently over time for it then to behave in a  
100 ductile manner by plate stretching, prior to the development of a new mid-ocean spreading  
101 centre.

102

## 103 **2. Mathematical Model**

104 The thermal evolution of a vertical dyke intruded into continental crust (Figure 2) is modelled  
105 by solving the two-dimensional (2D) heat flow equation both horizontally ( $x$ -direction) and in  
106 depth ( $z$ ). The model is set up in a similar manner to previous studies (Royden et al., 1980;  
107 Buck, 2004; Buck et al., 2005; Bialas et al., 2010) with a vertical cross-section through the  
108 crust incorporating a model rift axis where consecutive dykes intrude along the centre of the  
109 previous one. The dykes are intruded at a time-averaged rate which is constant at all depths  
110 ( $z$ ) beneath the rift axis. Homogeneous composition continental crust is assumed, such that  
111 thermal conductivity ( $K$ ), diffusivity ( $\kappa$ ), density ( $\rho$ ), specific heat capacity ( $C_p$ ) and latent heat  
112 of fusion ( $L$ ) remain constant as a function of depth and temperature. The 2D heat-flow  
113 equation, incorporating the latent heat of fusion is

$$114 \quad \rho C_p \frac{\partial T}{\partial \tau} + \rho L \frac{\partial X}{\partial \tau} = K \nabla^2 T$$

115 **Equation 1**

116 where  $\nabla^2 = \frac{\partial^2}{\partial x^2} + \frac{\partial^2}{\partial z^2}$ ,  $T(x, z, \tau)$  is the temperature,  $X(x, z, \tau)$  is the melt fraction and  $\tau$  is the  
117 time (e.g., Turcotte and Schubert 2002). Melt fraction is assumed to depend only on  
118 temperature such that

$$119 \quad X = F(T)$$

120 **Equation 2**

121 where  $F$  is a function derived from a simple three-component phase diagram based on a  
122 Hawaiian olivine tholeiite basalt (Sample 14, Yoder and Tilley 1962) with three components;  
123 the chemical analysis was recalculated as a CIPW norm (Cox et al. 1979) and the  
124 components were re-normalised to give olivine, clinopyroxene and plagioclase. The melt  
125 fractions corresponding to temperatures in the range 0 to 1320°C were calculated using the  
126 simulated phase equilibria model of Witham (2008). The simple three-phase system was  
127 used to test the model's performance when compared with analytical solutions, and to

128 explore the effects of different parameters.  $F$  (Equation 2) is generally determined from  
129 experimental studies. Here, it is approximated by a series of linear trends.

130 The far-field geotherm  $T(z)$  is assumed to satisfy the boundary conditions

131 
$$T \rightarrow \frac{Q_0}{K} z - \frac{A}{2K} z^2 \text{ as } x \rightarrow \pm \infty$$

132 **Equation 3**

133 where the surface temperature is taken to be zero. This equation is valid for all values of  $z$ .

134 The initial condition for a single injection is

135 
$$T = T_m, \quad |x| < \omega; \quad T = \frac{Q_0}{K} z - \frac{A}{2K} z^2, \quad |x| > \omega \quad \text{at } \tau = 0$$

136 **Equation 4**

137 for  $z_0 \leq z \leq z_1$ , where  $z_0$  and  $z_1$  define the upper and lower surfaces of the modelled region of  
138 the crust (Figure 2) and whose temperature satisfies Equation (3) such that

139 
$$T = \frac{Q_0}{K} z_0 \text{ at } z = z_0 \text{ and } T = \frac{Q_0}{K} z_1 \text{ at } z = z_1, T_m \text{ is the magma injection temperature at}$$

140 time  $\tau = 0$  and  $2\omega$  is the dyke width. Above and below the intruded region ( $z < z_0$  and  $z > z_1$ ),

141 the thermal evolution of the crust is governed by the geotherm (Equation 3). Solutions of

142 Equations (1) – (4) are required to determine how the temperature and melt fraction evolve

143 as functions of  $x$ ,  $z$ , and  $\tau$ . Numerical solutions of Equations (1) – (4) were determined using

144 an explicit finite difference method. A full description of the finite difference method is

145 included as an appendix.

146 The heat-flow equation (Equation 1) was discretised using forward difference

147 approximations in  $\tau$  and a central difference approximation in  $x$ . The solution was computed

148 forwards in time by incrementing the timestep ( $k$ ) through integer values, starting with  $k = 0$

149 where  $T$  and  $X$  are determined by the initial temperature profile (Equation 6). Due to the

150 symmetrical nature of the solution about  $x = 0$ , the computational domain was restricted to

151 positive  $x$  values and a symmetry condition applied to the left hand edge of the domain.  
152 Successive intrusions of basalt at a constant injection rate were modelled numerically by  
153 displacing previously computed values of temperature rightwards (mimicking advection) by  
154 the half-dyke width at each new injection time and inserting the new intrusion of the same  
155 dyke width and temperature  $T_m$  in the space vacated. The advection of heat due to ductile  
156 stretching of the crust is not considered in our models since it will be negligible over the  
157 time-scales we model intrusions. Brittle deformation by faulting has also not been accounted  
158 for in the model. The injection frequency  $\psi$  was defined as the ratio of the magmatic  
159 extension rate  $S$  to the dyke thickness  $2\omega$  so that  $S = 2\omega\psi$ .

160

### 161 **3. Specific Model Parameterisation for Ethiopia**

162 The tectonically active East African Rift (EAR) and southern Red Sea Rift (RSR) in Ethiopia  
163 provide an excellent opportunity to source realistic input parameters for our thermal model  
164 (Figure 1). The starting composition was established using the lava from a 2007 fissure  
165 eruption in Afar (sample A2, Ferguson et al. 2010), with a water content of 0.4 wt% assumed  
166 at all depths. The series of linear fits used for the temperature-melt fraction relationship  
167 were determined using the MELTS (Ghiorso and Sack 1995, Asimow and Ghiorso 1998)  
168 and Rhyolite-MELTS (Gualda et al. 2012) thermodynamic modelling programs. The  
169 composition of the injected material and the intruded crust are assumed to be the same.  
170 Because the injected material mainly cools and the host rock predominantly slowly increases  
171 in temperature, the temperature-melt fraction relationship of the host material is not  
172 important and will not affect the temperatures produced (Daniels, 2012). The solidus  
173 temperature was based on previously published model temperatures (Annen and Sparks  
174 2002).

175 The temperature-melt fraction relationship was calculated for four different pressures  
176 corresponding to different depths in the crust:  $z = 5, 10, 15$  and  $20$  km (Figure 3). It has



177 been inferred from wide-angle seismic (Maguire et al., 2006), gravity (Cornwell et al., 2006)  
178 and electrical resistivity (Desissa et al., 2013) study in Ethiopia that gabbroic intrusions occur  
179 in this depth range in the upper crust beneath Quaternary-Recent zones of magmatic  
180 extension. Partial melt is also known to reside at these depths, as revealed by  
181 magnetotelluric analysis of the subsurface (Whaler and Hautot, 2006). The lithostatic  
182 pressures and corresponding depths (calculated using  $\rho gh$  with  $\rho = 2800 \text{ kg/m}^3$ , Annen and  
183 Sparks 2002), along with all of the crystallisation points, are in Table 1. Values of the  
184 physical parameters assumed are summarised in Table 2. A dyke thickness of 15 m allowed  
185 different extension rates  $S$  to be achieved by varying the dyke injection frequency  $\psi$ .  
186 Previous models that varied dyke thickness and injection frequency whilst fixing extension  
187 rate have shown that thinner, more frequently intruded dykes increase the crustal  
188 temperature more quickly than thicker, less frequently intruded dykes, but the effect is  
189 insignificant compared with other parameters such as the extension rate (Daniels, 2012). It  
190 is for this reason that only one dyke thickness is chosen. Injection temperatures ( $T_m$ ) in the  
191 range 1240-1320°C were studied.

192

#### 193 **4. Results**

194 Two-dimensional model runs with  $x_0 = 0$ ,  $x_1 = 10 \text{ km}$ ,  $z_0 = 0$ ,  $z_1 = 10 \text{ km}$ ,  $\Delta x = \Delta z = 5 \text{ m}$  and  
195 dyke width = 15 m were conducted for extension rates of 5, 10, 15 and 20 mm/yr and for a  
196 duration of 200 ka. In these models, the injected dyke extended over the depth of the  
197 computational array. Figure 4 shows the output of these two-dimensional models and the  
198 brittle-ductile transition (black line) and solidus (red line) isotherms migrating across the  
199 computational domain. Loss of heat at the top and bottom of the domain can be seen to  
200 affect the temperatures.

201 As detailed in the supplementary material, the model was tested successfully against  
202 independent analytical solutions. Moreover, except at the top and bottom of the model, this

203 2D numerical model can be approximated by a 1D model where the temperature profile  
204 depends only on the horizontal distance  $x$  at a given, constant depth  $z$ : both 1D and 2D  
205 numerical models yield similar solutions (see the supplementary material for details).  
206 However, at the top and bottom of the modelled region of the crust, the thermal boundary  
207 conditions influence the solution there immediately and eventually affect the solution  
208 throughout the model space. But, if these upper and lower boundaries ( $z_0$  and  $z_1$ ) are  
209 sufficiently far apart, the 1D model yields a very good approximation for the model interior,  
210 thus reducing computational time considerably.

211 At the top of the 2D model, the boundary effect is analogous to the surface cooling of the  
212 system (see the supplementary materials for details). The amount of the modelled crust  
213 affected after time  $\tau$  can be approximated using  $\ell^2 \sim \kappa\tau$  such that after 1 Ma, the top 4 km of  
214 the crust will have experienced surface cooling, increasing to 7 km after 3 Ma. For depths  
215  $>5$  km, the 1D heat flow equation is thus appropriate for the study of the thermal structure of  
216 continental crust during extension by dyke intrusion over a time period of a couple of Ma.

217 The 1D numerical model was run using the parameters in Table 2 for extension rates of 3, 5,  
218 10, 20, and 25 mm/yr, for a horizontal range of  $x_0 = 0$  to  $x_1 = 30$  km and at depths ( $z$ ) of 5,  
219 10, 15, and 20 km. These extension rates were designed to encompass the  $\sim 6$  mm/yr  
220 extending MER, and the  $\sim 16.4$  mm/yr extending RSR in Afar. Each model was run for 5 Ma,  
221 with temperature monitored as a function of distance from dyke injection point. Particular  
222 attention was paid to the solidus temperature and brittle-ductile transition ( $600^\circ\text{C}$ ) isotherms.  
223 Magmatic extension rate and the time taken to reach the solidus temperature or the brittle-  
224 ductile  $600^\circ\text{C}$  isotherm at the injection position ( $x=0$ ) display an inverse power law  
225 relationship ( $S$  is proportional to  $\frac{1}{\sqrt{t}}$ ; Figures 5 and 6). Thus, magmatic extension rate is  
226 approximately proportional to  $\frac{1}{\sqrt{t}}$ , independent of injection temperatures (Figure 5). Injection  
227 temperature is thus secondary to extension rate in governing the rate of temperature  
228 increase.

229 The distance ( $x$ ) from the dyke injection and the time taken to reach a given isotherm  
230 correlate linearly for all extension rates ( $S$ ) (Figure 7 A). The linear trend indicates that the  
231 magmatic extension rate is dominant at distances close to the dyke injection location.  
232 Figure 7 B shows modelled isotherm positions as a function of distance from the dyke  
233 injection point; also shown are isotherm positions determined from extension rate alone  
234 (effects of conduction are close to negligible). Extension rate is a good proxy for isotherm  
235 migration rate in the near field, but with increasing distance from the injection point,  
236 conduction becomes an increasingly important additional effect.

237 When the time is plotted as a function of extension rate (Figure 6), the results are  
238 comparable with the results of Michaut and Jaupart (2006) who found that the critical  
239 temperature in their numerical models ( $t_c$ ) was inversely proportional to injection rate  
240 squared ( $Q^2$ ). The constant that multiplies the injection rate in Michaut and Jaupart (2006)  
241 and the extension rate in each of the relationships in Figure 6 is dependent on the  
242 parameters used in the modelling (Table 2) and therefore is different for each case.  
243 However, in both this study and in Michaut and Jaupart (2006), the time taken to reach a  
244 particular temperature is inversely proportional to the square of the extension rate. The  
245 timescales for the build up of temperature calculated for different magmatic extension rates  
246 are quite varied. Calculations show that it will take significantly longer for the ambient  
247 temperature to build up at slower extension rates: an extension rate three times faster will  
248 decrease this time by an order of magnitude (Figure 5).

249

## 250 **5. Discussion**

### 251 **5.1. Overview**

252 It is now well established that dyke intrusion achieves a significant proportion of extension  
253 during continental rifting (e.g., Maguire et al., 2006; Thybo and Nielsen, 2009; White et al.,  
254 2008), yet relatively little attention has been paid in the rifting community to the effects this

255 has on the thermal evolution (and by inference the strength) of the continental crust during  
256 breakup. Previous studies have demonstrated that appreciable crustal heating occurs due  
257 to repeated magma intrusion in arc settings (e.g. Annen et al. 2006, Solano et al. 2012), and  
258 a similar thermal modelling approach has been followed in this study of continental rifting.

259 This study demonstrates that the thermal structure of the crust is controlled by several  
260 factors: intrusion depth, injection temperature, and magmatic extension rate. Of these,  
261 magmatic extension rate exerts first order control on crustal thermal structure (Figures 5, 6  
262 and 7). The rate of transfer of heat laterally away from the zone of dyke intrusion can be  
263 approximated in the near-field by the magmatic extension rate, but at greater distances (>3-  
264 4 km), cooling by conduction becomes an important factor (Figure 7).

265 The location of the injection relative to the previous injection is also likely play a role in the  
266 timescale of the build-up of heat in the crust. Here, each successive injection has intruded  
267 through the centre of the previous injection. This may have had the effect of insulating each  
268 hot injection from the cooler crust to either side and therefore indicate that the timescales  
269 calculated represent minimum estimates. Additionally, the advection of heat due to ductile  
270 stretching of the crust has not been accounted for in the model. At slow extension rates  
271 relevant for continental rift zones, this effect is negligible compared to the marked and rapid  
272 heating caused by intrusion. At faster rates of extension observed at mid-ocean ridges, but  
273 rare for continental rifts, the advection of heat is likely more important.

274 Observations of seismicity worldwide indicate strongly that earthquake depths are  
275 fundamentally limited by the brittle-ductile transition in continental crust and commonly the  
276 600°C isotherm is used to mark this transition in typical crust (e.g., Maggi et al., 2000a,b;  
277 Jackson, 2002). A 10-20 km wide region of the crust would be expected to heat to above  
278 600°C in <1 Ma, even at relatively slow extension rates of ~10 mm/yr (Figure 7). At slower  
279 rates, heating to 600°C will take much longer (e.g., 6.3 Ma for a 20 km-wide region at 3  
280 mm/yr).

281           5.2. Implications for the thermal development of the MER

282   The MER is the northern-most sector of the EAR and displays several stages of rift sector  
283   development along strike. Embryonic continental rifting in the southern MER is dominated  
284   by border faulting while in the northern MER, rifting is more evolved and axial magma  
285   intrusion contributes significantly to Nubia-Somalia separation (e.g., Hayward and Ebinger  
286   1996; Kogan et al., 2012). The northern MER has also undergone considerable  
287   development over time: initial rifting during Miocene times was characterised by upper-  
288   crustal extension accommodated by the large-offset border faults that define the rift valley  
289   flanks today (e.g., Wolfenden et al., 2005). Since Quaternary times however, faulting and  
290   volcanism have localized to the 20-30 km wide WFB axial zone. Aligned Quaternary-Recent  
291   monogenetic basaltic cones and resultant lava flows cut by the most active faults within the  
292   MER, coupled with geodetic evidence that ~80% of Nubia-Somalia plate separation is  
293   presently accommodated within the WFB (Bilham et al., 1999), was cited by Ebinger and  
294   Casey (2001) as evidence that a significant proportion of extension in the MER is achieved  
295   by episodic magma intrusion. More recent studies of GPS measurements acquired over the  
296   last two decades confirm the MER is currently opening at 5-6 mm/yr in an ESE-WNW  
297   direction (Kogan et al., 2012). The seismic moment release in the MER since 1960 is  
298   around half that expected from the plate separation velocities, which suggests 50% of the  
299   extension is accommodated by aseismic processes such as magma intrusion (Hofstetter  
300   and Beyth, 2003).

301   The 2001-2003 Ethiopia Afar Geoscientific Lithospheric Experiment (see Bastow et al., 2011  
302   for a review) has facilitated the development of high-resolution sub-surface geophysical  
303   models of the MER. Wide-angle active-source, passive-seismic, and gravity studies of  
304   crustal structure have shown that zones of Quaternary-Recent magmatism in the WFB are  
305   underlain by anomalously high P-wavespeed and high-density material compared to  
306   surrounding native continental crust (e.g., Keranen et al., 2004; Mackenzie et al., 2005; Daly  
307   et al., 2008; Cornwell et al., 2006; Maguire et al., 2006; Tiberi et al., 2005). These are

308 interpreted as zones of localised gabbroic intrusions that extend from the aligned  
309 monogenetic cone fields along the rift axis surface to the base of the crust at 30-35 km depth  
310 (e.g., Keranen et al., 2004; Mackenzie et al., 2005). While the total volume of new intruded  
311 material beneath the axis is debated, the marked reduction in seismic velocities in the upper  
312 ~8 km of the crust suggests intrusion contributes a lower proportion of extension at these  
313 shallow depths compared to elsewhere in the crust (Keranen et al., 2004).

314 The thermal models developed in this study show that ~6 mm/yr extension in the MER  
315 should, if achieved 100% by magma intrusion, by now have heated the crust to  
316 temperatures in excess of 600°C (Figures 5 and 7). Observations of seismicity in the MER  
317 render this hypothesis implausible, however. Variations in seismicity along the WFB instead  
318 demonstrate along-axis variability in the thermal state of the crust. The Boset segment  
319 (Figure 1) is the most magmatically active portion of the MER (e.g. Abebe et al., 2007) and  
320 accordingly exhibits the least seismicity and shallowest brittle-ductile transition at 6-9 km  
321 depth (Beutel et al., 2010). Crustal tomographic studies indicate the highest P-wavespeed  
322 anomalies anywhere along the MER occur in the Boset segment, with the implication that  
323 the crust here contains a higher proportion of new igneous material than elsewhere along  
324 the rift (e.g. Keranen et al., 2004; Maguire et al., 2006). In other areas of the MER, with  
325 lower amplitude high P-wavespeed anomalies, seismicity is evident to depths of 15-18 km,  
326 indicating higher crustal strength and lower temperatures (Beutel et al., 2010).

327 If only 50% of the 6 mm/yr extension in the MER has been achieved by dyke intrusion  
328 beneath the WFB, the thermal models presented in this study would predict a significantly  
329 smaller degree of heating and weakening. Extrapolating from Figure 7, a zone 20 km wide  
330 would heat to the brittle-ductile transition at all depths only after about 6 Ma. This is a longer  
331 period of time than the WFB has existed within the MER: earlier extension was confined to  
332 the large-offset border faults (Wolfenden et al., 2005). The depth extent of seismicity and  
333 variations in P-wave speeds beneath the magmatic segment along the axis of the MER  
334 when interpreted in light of our thermal modelling supports the interpretation that the crust

335 beneath the WFB is not 100% new mafic material. Rather it is a zone of heavily intruded  
336 continental crust. Mechanical extension (faulting and stretching) thus remains an important  
337 mechanism of strain accumulation between Nubia and Somalia.

### 338 5.3 Implications for the development of continent-ocean transition

339 In contrast to the relatively young magmatic phase of extension observed in the MER, Afar  
340 has experienced magma assisted rifting since the Miocene (Wolfenden et al. 2005). Our  
341 models predict that given the higher extension rate (~16 mm/yr) and longer period of time  
342 elapsed since the onset of magma intrusion, crustal temperatures should be too high for  
343 brittle deformation to occur; the crust should thus now be able to deform in a ductile manner  
344 (stretching). However, most of sub-aerial Afar has generally thick crust (Makris and  
345 Ginzburg, 1987; Hammond et al., 2011), and is still seismically active (Ayele et al., 2007a,b;  
346 Keir et al., 2011a,b; Ebinger et al., 2013) indicating that magma intrusion has not thermally  
347 weakened the plate as much as suggested by the model. A simple explanation for this is  
348 that the Arabia-Nubia plate boundary has shifted north-eastward several times in response  
349 to triple junction development in Afar. During earlier phases of magma-assisted rifting in  
350 Miocene times, strain was accommodated in magmatic segments located proximal to the  
351 western southern Red Sea border fault on the western margin of Afar (e.g. Wolfenden et al,  
352 2005). Since then, strain has localised progressively north-eastward to form the current  
353 configuration of axial volcanic segments (e.g. Dabbahu and Harraro segments) and  
354 sometimes amagmatic grabens (e.g. Tendaho; Dobi and Hanle graben: Tesfaye et al.,  
355 2003). Consequently, magma intrusion is unlikely to have been localised for long enough in  
356 any given location for sufficient crustal heating to occur. As a result, extension by dyke  
357 intrusion remains the optimal straining mechanism (e.g., Buck, 2006), with plate strength  
358 likely still too high to permit significant ductile stretching localised around the intrusion zone.

359 Our thermal models show that only when dyke intrusion is focused to one magmatic  
360 segment for a protracted period of time would aseismic ductile deformation be expected to

361 commence (Figures 5 and 7). One region where this transition may be underway is the sub-  
362 aerial but below sea-level Danakil depression in northernmost Afar. Here rapid basin  
363 subsidence since ~5 Ma indicated by 3-5 km accumulations of Pliocene-Recent sediments,  
364 combined with a pulse of Quaternary-Recent fissural basaltic volcanism, were interpreted by  
365 Bastow and Keir (2011) as evidence for a late stage of plate stretching and an increase in  
366 decompression melting in the mantle. The Bastow and Keir (2011) study lacked constraint  
367 on the mechanism responsible for the shift from extension by magma intrusion to extension  
368 by ductile stretching, but noted that late-stage subsidence and volcanism is a common  
369 feature of the geological record at magmatic rifted margins globally. The thermal models  
370 presented in this study show that at the ~10 mm/yr extension rates observed in the Danakil  
371 depression (McClusky et al, 2010), a 20 km wide zone will be sufficiently heated at 5 km  
372 depth after about 1 Ma of extension by magma intrusion to deform in a ductile fashion  
373 (Figure 7). However, in the Danakil depression where plate stretching has commenced,  
374 heat advection is likely to be a considerable additional component. A hotter and weaker  
375 plate in the Danakil depression is supported by earthquakes restricted to the upper ~5 km of  
376 the crust (e.g., Craig et al., 2011; Nobile et al., 2012), and ~5 km effective elastic plate  
377 thickness derived from gravity-topography coherence studies of plate strength (Ebinger and  
378 Hayward, 1996; Perez-Gussinye et al., 2009). When synthesized in light of a priori  
379 geoscientific constraints from the Danakil region, our thermal models thus indicate that a  
380 late-stage of localised plate stretching, with an associated pulse of decompression melting,  
381 can readily characterise the final stages of continent to ocean transition.

382

## 383 **6 Conclusions**

384 We have developed a numerical solution to the heat-flow equation to quantify the effects of  
385 dyke intrusion on the thermal structure of the crust during rifting, and on the timescales of  
386 the heating at varying magmatic extension rates. The rate of extension by intrusion is shown



387 to exert first order control on crustal thermal structure, and when extension is achieved  
388 entirely by dyke intrusion, the crust is expected to heat considerably on time-scales of less  
389 than 1 Ma.

390 We benchmarked our thermal models against recently developed constraints on crustal  
391 structure and dyke intrusion episodes in Ethiopia. For the MER, our model predicts brittle  
392 deformation at the ultra-slow extension rates of ~6 mm/yr will cease after only 300 ka of  
393 entirely magmatic extension localised to the rift axis. Our thermal calculations, corroborated  
394 by observations of seismic moment release, depth extent of seismicity, and P-wave speeds,  
395 point instead to a rifting model by which only ~50% of the extension is accommodated by  
396 magma intrusion. In the Danakil depression of northernmost Afar in contrast, a combination  
397 of faster extension rates of ~10 mm/yr and longer history of magma intrusion has likely  
398 resulted in sufficient heating and weakening of the plate to induce a late stage phase of  
399 localised ductile stretching near the intruded zone. Our results demonstrate the significant  
400 impact of dyke intrusion on the rheology of continental crust during rifting. The challenge  
401 now is to understand better how dyke intrusion affected plate strength during the  
402 development of magmatic margins worldwide.

403

#### 404 Acknowledgements

405 KAD would like to thank G. P. Daniels, P. G. Daniels and F. Witham for early assistance with  
406 the numerical coding and helpful discussions thereafter. C. Annen, J. D. Blundy, G. A. Jones  
407 and K. A. Whaler are also thanked for constructive comments and suggestions. The authors  
408 are grateful to three anonymous reviewers whose comments have strengthened and  
409 improved the manuscript. KAD was supported by a NERC Consortium Grant. RSJS is co-  
410 supported by a grant from the European Research Council. IDB is funded by the Leverhulme  
411 trust.

412

413 **References**

- 414 Abebe, B., Acocella, V., Kome, T., Ayalew, D., 2007. Quaternary faulting and volcanism in  
415 the Main Ethiopian Rift. *J. Afr. Earth Sci.* 48, 115-124.
- 416 Annen, C., Sparks, R.S.J., 2002. Effects of repetitive emplacement of basaltic intrusions on  
417 thermal evolution and melt generation in the crust. *Earth Planet. Sci. Lett.* 203, 937-955.
- 418 Annen, C., Blundy, J. D., and Sparks, R. S. J., 2006. The genesis of intermediate and silicic  
419 magmas in deep crustal hot zones. *J. Pet.* 47(3), 505-539.
- 420 Asimow, P.D., Ghiorso, M.S., 1998. Algorithmic Modifications Extending MELTS to Calculate  
421 Subsolidus Phase Relations. *American Mineralogist* 83, 1127-1131.
- 422 Ayele, A., Stuart, G., Bastow, I., Keir, D., 2007a. The August 2002 earthquake sequence in  
423 north Afar: Insights into the neotectonics of the Danakil microplate. *J. Af. Earth Sci.*, 48(2),  
424 70-79.
- 425 Ayele, A., Jacques, E., Kassim, M., Kidane, T., Omar, A., Tait, S., Nercessian, A.,  
426 deChabaliere, J-B. and King, G., 2007b. The volcano-seismic crisis in Afar, Ethiopia, starting  
427 September 2005. *Earth Planet. Sci. Lett.* 255, 177-187.
- 428 Bastow, I.D., Nyblade, A.A., Stuart, G.W., Rooney, T., Benoit, M.H., 2008. Upper Mantle  
429 Seismic Structure Beneath the Ethiopian Hotspot: Rifting at the Edge of the African Low  
430 Velocity Anomaly. *Geochem. Geophys. Geosyst.*, 9(12), doi:10.1029/2008GC002107.
- 431 Bastow, I.D., Keir, D., 2011. The protracted development of the continent ocean transition in  
432 Afar. *Nature Geoscience* 4, 248-250.
- 433 Bastow, I.D., Keir, D., Daly, E., 2011. The Ethiopia Afar Geoscientific Lithospheric  
434 Experiment (EAGLE): Probing the transition from continental rifting to incipient seafloor  
435 spreading. In *Volcanism and Evolution of the African Lithosphere* (Beccaluva, L., Bianchini,

436 G., and Wilson, M., Editors). *Geol. Soc. Am. Spec. Papers* 478, 51-76,  
437 doi:10.1130/2011.2478(04).

438 Beutel, E., van Wijk, J., Ebinger, C., Keir, D., Agostini, A., 2010. Formation and stability of  
439 magmatic segments in the Main Ethiopian and Afar rifts. *Earth Planet. Sci. Lett.* 293, 225-  
440 235.

441 Bialas, R. W., Buck, W. R., and Qin, R., 2010. How much magma is required to rift a  
442 continent? *Earth Planet. Sci. Lett.* 292, 68-78.

443 Bilham, R., Bendick, R., Larson, K., Mohr, P., Braun, J., Tesfaye, S., Asfaw, L., 1999.  
444 Secular and Tidal Strain Across the Main Ethiopian Rift. *Geophys. Res. Lett.* 26 (18), 2789-  
445 2792.

446 Bohron, W. A., Spera, F. J., 2001. Energy-Constrained Open-System Magmatic Processes  
447 II: Application of Energy-Constrained Assimilation-Fractional Crystallisation (EC-AFC) Model  
448 to Magmatic Systems. *J. Pet.* 42 (5), 1019-1041.

449 Buck, W. R., 2004. Consequences of asthenospheric variability on continental rifting. In  
450 *Rheology and Deformation of the Lithosphere at Continental Margins* (Karner, G. D., et al.,  
451 Editors), Columbia University Press.

452 Buck, W., 2006, The role of magma in the development of the Afro-Arabian Rift System, in  
453 *The Structure and Evolution of the East African Rift System in the Afar Volcanic Province*,  
454 eds. Yirgu, G. Ebinger, C.J., Maguire, P.K.H., *Geol. Soc. Lond. Spec. Pub.*, 259, 43-54.

455 Buck, W. R., Lavier, L. L., and Poliakov, A. N. B., 2005. Modes of faulting at mid-ocean  
456 ridges. *Nature* 434, 719-723.

457 Carslaw, H.S., Jaeger, J.C., 1950. *Conduction of Heat in Solids*. Oxford University Press.

458 Cornwell, D.G., Mackenzie, G.D., England, R.W., Maguire, P.K.H., Asfaw, L.M., Oluma, B.,  
459 2006. Northern Main Ethiopian Rift crustal structure from new high-precision gravity data. In

460 The Afar Volcanic Province within the East African Rift System (Yirgu, G., Ebinger, C. J.,  
461 Maguire, P. K. H., Editors). Geol. Soc. Lond. Spec. Pub. 259, 307-321.

462 Cox, K.G., Bell, J.D., Pankhurst, R.J., 1979. The Interpretation of Igneous Rocks. George  
463 Allen and Unwin.

464 Craig, T. J., Jackson, J. A., Priestley, K., and McKenzie, D., 2011. Earthquake distribution  
465 patterns in Africa: their relationship to variations in lithospheric and geological structure, and  
466 their rheological implications. *Geophys. J. Int.* 185(1), 403-434.

467 Daly, E., Keir, D., Ebinger, C.J., Stuart, G.W., Bastow, I.D. and Ayele, A., 2008. Crustal  
468 tomographic imaging of a transitional continental rift: the Ethiopian rift. *Geophys. J. Int.*  
469 172(3), 1033-1048.

470 Daniels, K., 2012. Modelling magma transport: a study of dyke injection. Ph.D. thesis,  
471 University of Bristol.

472 Desissa, M., Johnson, N. E., Whaler, K. A., Hautot, S., Fisseha, S., Dawes, G. J. K., 2013. A  
473 mantle magma reservoir beneath an incipient mid-ocean ridge in Afar, Ethiopia. *Nat. Geosci.*  
474 In press.

475 Ebinger, C. J., Hayward, N. J., 1996. Soft plates and hot spots: Views from Afar. *J.*  
476 *Geophys. Res.* 101, (B10), 21859–21876.

477 Ebinger, C.J., Casey, M., 2001. Continental breakup in magmatic provinces: An Ethiopian  
478 example. *Geology* 29, 527-530.

479 Ebinger, C.J., van Wijk, J., Keir, D., 2013. The time scales of continental rifting: Implications  
480 for global processes. *Geological Society of America Special Paper*, 500,  
481 doi:10.1130/2013.2500(11).

482 Ferguson, D.J., Barnie, T.D., Pyle, D.M., Oppenheimer, C., Yirgu, G., Lewi, E., Kidane, T.,  
483 Carn, S., Hamling, I., 2010. Recent rift-related volcanism in Afar, Ethiopia. *Earth Planet. Sci.*  
484 *Lett.* 292, 409-418.

485 Ferguson, D.J., MacLennan, J., Bastow, I.D., Pyle, D.M., Jones, S.M., Keir, D., Blundy, J.,  
486 Plank, T., Yirgu, G. Melting during late-stage rifting in Afar is hot and deep. *Nature* 499, 70-  
487 73 (doi:10.1038/nature12292).

488 Ghiorso, M.S., Sack, R.O., 1995. Chemical Mass Transfer in Magmatic Processes. IV. A  
489 Revised and Internally Consistent Thermodynamic Model for the Interpolation and  
490 Extrapolation of Liquid-Solid Equilibria in Magmatic Systems at Elevated Temperatures and  
491 Pressures. *Contrib. Min. Pet.* 119, 197-212.

492 Grandin, R., Jacques, E., Nercessian, A., Ayele, A., Doubre, C., Socquet, A., Keir, D.,  
493 Kassim, M., Lemarchand, A., King, G. C. P., 2011. Seismicity during lateral dike  
494 propagation: Insights from new data in the recent Manda Hararo–Dabbahu rifting episode  
495 (Afar, Ethiopia). *Geochem. Geophys. Geosyst.* 12(4), Q0AB08.

496 Gualda, G.A.R., Ghiorso, M.S., Lemons, R.V., Carley, T.L., 2012. Rhyolite-MELTS: A  
497 modified calibration of MELTS optimized for silica-rich, fluid-bearing magmatic systems. *J.*  
498 *Pet.* 53(5), 875-890.

499 Hammond, J.O.S., Kendall, J-M., Stuart, G.W., Keir, D., Ebinger, C., Ayele, A., Belachew,  
500 M., 2011. The nature of the crust beneath the Afar triple junction: Evidence from receiver  
501 functions. *Geochem. Geophys. Geosyst.* 12, Q12004.

502 Hayward, N. J., Ebinger, C., 1996. Variations in the along-axis segmentation of the Afar Rift  
503 system. *Tectonophysics* 15(2), 244-257.

504 Hofstetter, R., Beyth, M., 2003. The Afar Depression: Interpretation of the 1960-2000  
505 earthquakes. *Geophys. J. Int.* 155, 715-732.

506 Jackson, J., 2002. Strength of the continental lithosphere: Time to abandon the jelly  
507 sandwich? *GSA Today*, September, 4-9.

508 Jaupart, C., and Mareschal, J-C., 2007. Heat flow and thermal structure of the lithosphere. In  
509 *Crust and Lithosphere Dynamics* (Watts, A. B., Editor), *Treatise on Geophysics* 6, 217–250.

510 Jaupart, C., and Mareschal, J-C., 2011. *Heat Generation and Transport in the Earth*.  
511 Cambridge University Press.

512 Keir, D., Hamling, I.J., Ayele, A., Calais, E., Ebinger, C., Wright, T.J., Jacques, E.,  
513 Mohammed, K., Hammond, J.O.S., Belachew, M., Baker, E., Rowland, J.V., Lewi, E.,  
514 Bennati, L., 2009. Evidence for focussed magmatic accretion at segment centres from lateral  
515 dike injections captured beneath the Red Sea Rift in Afar. *Geology* 37(1), 59-62.

516 Keir, D., Belachew, M., Ebinger, C., Kendall, J-M., Hammond, J.O.S., Stuart, G.W., Ayele,  
517 A., Rowland, J.V., 2011a. Mapping the evolving strain field during continental breakup from  
518 crustal anisotropy in the Afar Depression. *Nature Communications* 2:285, doi:  
519 10.1038/ncomms1287.

520 Keir, D., Pagli, C., Bastow, I., Ayele, A., 2011b. The magma-assisted removal of Arabia in  
521 Afar: Evidence from dike injection in the Ethiopian rift captured using InSAR and seismicity.  
522 *Tectonophysics* 30, TC2008, doi:10.1029/2010TC002785.

523 Keir, D., Bastow, I., Pagli, C., Chambers, E.L., 2013. Spatial and temporal constraints on  
524 mechanisms of continental breakup: evidence from Afar. *Tectonophysics*,  
525 doi:10.1016/j.tecto.2012.10.015.

526 Keranen, K., Klemperer, S.L., Gloaguen, R., Group, E.W., 2004. Three-dimensional seismic  
527 imaging of a protoridge axis in the main Ethiopian rift. *Geology* 32, 949-952.

528 Kogan, L., Fisseha, S., Bendick, R., Reilinger, R., McClusky, S., King, R., and Solomon, T.,  
529 2012. Lithospheric strength and strain localization in continental extension from observations  
530 of the East African Rift. *J. Geophys. Res.* 17, B03402.

531 Laube, N., Springer, J., 1998. Crustal melting by ponding of mafic magmas: A numerical  
532 model. *J. Volc. Geotherm. Res.* 81, 19-35.

533 Mackenzie, G.D., Thybo, H. and Maguire, P.K.H., 2005. Crustal velocity structure across the  
534 Main Ethiopian Rift: Results from 2-dimensional wide-angle seismic modelling. *Geophys. J.*  
535 *Int.* 162, 994-1006.

536 Maggi, A., Jackson, J., McKenzie, D., Priestley, K., 2000a. Earthquake focal depths,  
537 effective elastic thickness, and the strength of the continental lithosphere. *Geology* 28, 495-  
538 498.

539 Maggi, A., Jackson, J., Priestley, K., Baker, C., 2000b. A reassessment of focal depth  
540 distributions in southern Iran, the Tien Shan and northern India: Do earthquakes really occur  
541 in the continental mantle? *Geophys. J. Int.* 143, 629-661.

542 Maguire, P.K.H., Keller, G.R., Klemperer, S.L., Mackenzie, G.D., Keranen, K., Harder, S.,  
543 O'Reilly, B., Thybo, H., Asfaw, L., Khan, M.A., Amha, M., 2006. Crustal structure of the  
544 northern Main Ethiopian Rift from the EAGLE controlled source survey; a snapshot of  
545 incipient lithospheric break-up. In *The Afar Volcanic Province within the East African Rift*  
546 *System* (Yirgu, G., Ebinger, C. J., Maguire, P. K. H., Editors). *Geol. Soc. Lond. Spec. Pub.*  
547 259, 271-293.

548 Makris, J., Ginzburg, A., 1987. The Afar Depression: transition between continental rifting  
549 and sea-floor spreading. *Tectonophysics* 141, 199-214.

550 McClusky, S., Reilinger, R., Ogubazghi, G., Amleson, A., Healeb, B., Vernant, P., Sholan, J.,  
551 Fisseha, S., Asfaw, L., Bendick, R., and Kogan, L., 2010. *Geophys. Res. Lett.* 37, L05301.

552 Michaut, C., Jaupart, C., 2006. Ultra-rapid formation of large volumes of evolved magma.  
553 *Earth Planet. Sci. Lett.* 250 (1-2), 38-52.

554 Mohr, P.A., 1967. Major volcanotectonic lineament in the Ethiopian Rift System. *Nature* 213,  
555 664-665.

556 Nobile, A., Pagli, C., Keir, D., Wright, T. J., Ayele, A., Ruch, J. and Acocella, V., 2012 Dike-  
557 fault interaction during the 2004 Dallol intrusion at the northern edge of the Erta Ale Ridge  
558 (Afar, Ethiopia). *Geophys. Res. Lett.* 39(19), L19305.

559 Pérez-Gussinyé, M., Metois, M., Fernández, M., Vergés, J., Fulla, J., Lowry, A. R., 2009.  
560 Effective elastic thickness of Africa and its relationship to other proxies for lithospheric  
561 structure and surface tectonics. *Earth Planet. Sci. Lett.* 287(1), 152-167.

562 Rivers, M. L., Carmichael, I. S. E., 1987. Ultrasonic Studies of Silicate Melts. *J. Geophys.*  
563 *Res.* 92 (B9), 9247-9270.

564 Rooney, T.O., Herzberg, C., Bastow, I.D., 2012. Elevated mantle temperature beneath East  
565 Africa. *Geology*, 40(1), 27-30, G32382, [doi:10.1130/G32382.1](https://doi.org/10.1130/G32382.1)

566 Royden, L., Sclater, J.G., Von Herzen, R.P., 1980. Continental margin subsidence and heat  
567 flow: important parameters in formation of petroleum hydrocarbons. *Bull. Am. Assoc. Pet.*  
568 *Geol.* 64, 173-187.

569 Solano, J.M.S., Jackson, M.D., Sparks, R.S.J., Blundy, J.D., and Annen, C., 2012. Melt  
570 Segregation in Deep Crustal Hot Zones: a Mechanism for Chemical Differentiation, Crustal  
571 Assimilation and the Formation of Evolved Magmas. *J. Pet.* 53(10), 1999-2026.

572 Spera, F. J., 2000. Physical Properties of Magmas. In *Encyclopaedia of Volcanoes*  
573 (Sigurdsson, H., Editor-in-Chief). Academic Press, 1417 pp.

574 Stern, C. R., Wyllie, P. J., 1973. Water-saturated and undersaturated melting relations of a  
575 granite to 35 kilobars. *Earth Planet. Sci. Lett.* 18, 163-167.



576 Tesfaye, S., Harding, D.J., and Kusky, T.M., 2003. Early continental breakup boundary and  
577 migration of the Afar triple junction, Ethiopia. *GSA Bull.* 115(9), 1053-1067.

578 Thybo, H., Nielsen, C.A., 2009. Magma compensated crustal thinning in continental rift  
579 zones. *Nature* 457, doi:10.1038/nature07688, 873-876.

580 Tiberi, C., Ebinger, C., Ballu, V., Stuart, G.W. and Oluma, B., 2005. Inverse models of  
581 gravity data from the Red Sea-Aden-East African rifts triple junction zone. *Geophys. J. Int.*  
582 163(2), 775-787.

583 Turcotte, D. L., Schubert, G., 2002. *Geodynamics*. Cambridge University Press, pp 456.

584 Whaler, K.A., Hautot, S., 2006. The electrical resistivity structure of the crust beneath the  
585 northern Main Ethiopian Rift. In *The Afar Volcanic Province within the East African Rift*  
586 *System* (Yirgu, G., Ebinger, C.J., Maguire, P.K.H., Editors). *Geol. Soc. Lond. Spec. Pub.*  
587 259, 293-305.

588 White, R.S., Smith, L.K., Roberts, A.W., Christie, P.A.F., Kuszniir, N.J., the rest of the iSIMM  
589 Team, 2008. Lower crustal intrusion on the North Atlantic continental margin. *Nature* 452,  
590 doi:10.1038/nature06687, 460-464.

591 Witham, F., 2008. The degassing of basaltic magma chambers. Ph.D. thesis, University of  
592 Bristol.

593 Wolfenden, E., Ebinger, C., Yirgu, G., Renne, P., Kelley, S.P., 2005. Evolution of the  
594 southern Red Sea rift: birth of a magmatic margin. *Geol. Soc. Am. Bull.* 117, 846-864.

595 Wright, T.J., Ebinger, C., Biggs, J., Ayele, A., Yirgu, G., Keir, D., Stork, A., 2006. Magma-  
596 maintained rift segmentation at continental rupture in the 2005 Afar dyking episode. *Nature*  
597 42, 291-294.

598 Yoder, H.S., Tilley, C.E., 1962. *Origin of Basalt Magmas - An Experimental Study of Natural*  
599 *and Synthetic Rock Systems*. *J. Pet.* 3(3), 342-532.

600

601 **Figure captions**

602 Figure 1: Tectonic setting of the East African rift system in the Horn of Africa. Solid black  
603 lines show Oligocene-Miocene border faults of the Red Sea, Gulf of Aden and East African  
604 rifts. Red segments show the Quaternary-Recent subaerial rift axes. DD: Danakil  
605 Depression. TGD: Tendaho-Goba'ad Discontinuity. MS: magmatic segments. DG: Dobi  
606 Graben. HG: Hanli Graben. Dashed red lines are sea-floor spreading centres in the Red  
607 Sea and Gulf of Aden. Top left inset: topography of NE Africa and Arabia. Arrows show  
608 plate motions relative to a fixed Nubian plate. Red lines are plate boundaries.

609 Figure 2: A schematic diagram showing the set-up of the model relative to the overlying rift  
610 topography, and the dimensions and position of the computational domain within the crust.

611 Figure 3: Temperature versus melt fraction for 4 different pressures, calculated using  
612 MELTS (Ghiorso and Sack, 1995; Asimow and Ghiorso, 1998), Rhyolite-MELTS (Gualda et  
613 al., 2012) and experimental estimates of the water-saturated granite solidus (Stern and  
614 Wyllie, 1973; Annen and Sparks, 2002). Small differences in the melt fraction-temperature  
615 relationship will have a minimal effect on the results.

616 Figure 4: Outputs from two-dimensional model runs with  $z_0 = 0$  and  $z_1 = 10\text{km}$ , and  $\tau = 20$   
617 ka, 100ka and 200 ka. Above: extension rate  $S = 5$  mm/yr. Below:  $S = 20$  mm/yr. The brittle-  
618 ductile transition (black line) and solidus (red line) isotherms are highlighted.

619 Figure 5: Extension rate versus the time, expressed in ka, taken to reach the solidus and  
620  $600^\circ\text{C}$  isotherm temperatures at 5 km depth at the injection position. The extension rates of  
621 the MER ( $\sim 6$  mm/yr) and RSR (15 - 20 mm/yr) are highlighted. The injection temperatures  
622 are in the range  $T_m = 1220$  to  $1320^\circ\text{C}$ .

623 Figure 6: Time taken to reach the  $600^\circ\text{C}$  isotherm temperature as a function of extension  
624 rate.

625 Figure 7: A) Time taken to reach the solidus temperatures as a function of the distance away  
626 from the dyke injection point, at 5 km depth. B) The position of the 600°C isotherm (solid  
627 lines and unfilled dots) due to the model (lines) and the extension rate alone (dots). The  
628 component of the extension rate alone is calculated using the time taken to reach the 600°C  
629 isotherm at distance  $x = 0$  as the starting point, and then migrating the isotherm away from  
630 the starting point at the magmatic extension rate. Extension rates of 5 mm/yr (grey solid  
631 lines and unfilled dots) and 20 mm/yr (black solid lines and unfilled dots) are shown. The  
632 arrows show the components of extension alone (black arrow) versus the cooling due to  
633 conduction (grey arrow). The first arrow is much longer than the second one, illustrating that  
634 the time taken to reach the isotherm is primarily controlled by the extension rate; accounting  
635 for heat loss by conduction increases this time but this effect appears to be secondary.

636

### 637 **Table captions**

638 Table 1: Temperatures (T) in °C, and corresponding melt fractions (X) for four different  
639 pressures: 137.34 MPa (5 km depth); 274.68 MPa (10 km depth); 412.02 MPa (15 km  
640 depth); and 549.36 MPa-(20 km depth). Subscripts l, e and s correspond to the liquidus,  
641 eutectic and solidus temperatures respectively; c and c2 are arbitrary points on the X-T  
642 diagram chosen to give the best fit to the data.

643 Table 2: Nomenclature - Model parameters and input values. <sup>a</sup>Annen and Sparks (2002).

644 <sup>b</sup>Jaupart and Mareschal (2007). <sup>c</sup>Jaupart and Mareschal (2011).

645 Table 3: Time taken in years for the temperature at the injection line,  $x = 0$ , to reach the  
646 solidus temperature and the 600°C isotherm for different extension rates and depths.

647

### 648 **Supplementary Material**

649 **Practical Implementation of the Model**

650 Numerical solutions of Equations (1) – (4) were determined using an explicit finite difference  
 651 method. The heat-flow equation (Equation 1) was discretised using forward difference  
 652 approximations in  $\tau$  and a central difference approximation in  $x$  to give

$$\begin{aligned} \frac{T_{(i,j,k+1)} - T_{(i,j,k)}}{\Delta\tau} + C \frac{X_{(i,j,k+1)} - X_{(i,j,k)}}{\Delta\tau} \\ = \kappa \left( \frac{T_{(i+1,j,k)} - 2T_{(i,j,k)} + T_{(i-1,j,k)}}{(\Delta x)^2} \right. \\ \left. + \frac{T_{(i,j+1,k)} - 2T_{(i,j,k)} + T_{(i,j-1,k)}}{(\Delta z)^2} \right) \end{aligned}$$

653

654 **Equation A1**

655 where  $C = L / C_p$ . Here  $T_{(i,j,k)}$  and  $X_{(i,j,k)}$  are numerical approximations to  $T$  and  $X$  at location  $x$   
 656  $= i \Delta x$ ,  $z = z_0 + j \Delta z$  and time  $\tau = k \Delta \tau$  where  $\Delta x$ ,  $\Delta z$  and  $\Delta \tau$  are the step lengths in  $x$ ,  $z$  and  
 657  $\tau$  respectively. The modelled region of the crust is taken as  $-x_\infty \leq x \leq x_\infty$ ,  $z_0 \leq z \leq z_1$  where  $i$   
 658 ranges from  $-N$  to  $N$  with  $x_\infty = N \Delta x$ ;  $j$  ranges from 0 to  $M$  with  $z_1 - z_0 = M \Delta z$ .  $N$  and  $M$   
 659 are sufficiently large to accommodate the outer behaviour. Equation (5) can then be written  
 660 as

$$T_{(i,j,k+1)} + C X_{(i,j,k+1)} = R_{(i,j,k)}$$

661

662 **Equation A2**

663 where

$$\begin{aligned} R_{(i,j,k)} = T_{(i,j,k)} + C X_{(i,j,k)} + A (T_{(i+1,j,k)} - 2T_{(i,j,k)} + T_{(i-1,j,k)}) + B (T_{(i,j+1,k)} \\ - 2T_{(i,j,k)} + T_{(i,j-1,k)}) \end{aligned}$$

664

665 **Equation A3**

666 and  $A = \frac{\kappa \Delta \tau}{(\Delta x)^2}$ ,  $B = \frac{\kappa \Delta \tau}{(\Delta z)^2}$  and must be solved in conjunction with the  $X$ - $T$  relation

667 (Equation 2) in discretised form to find the solution values  $T_{(i,j,k+1)}$  and  $X_{(i,j,k+1)}$  at the new time-

668 step and each internal grid point  $(i,j)$ . With  $F$  of piecewise linear form,  $T_{(i,j,k+1)}$  and  $X_{(i,j,k+1)}$  can  
 669 be found exactly, depending on which linear section of  $F$  is relevant for any given value of  
 670  $R_{(i,j,k)}$ . Since Equation (8) describes a straight line of gradient  $-1 / C$ , its intersection with  
 671 Equation (2) is determined by the size of  $R_{(i,j,k)}$  relative to the value of  $R$  associated with each  
 672 crystallisation point. The new temperature and melt fraction are thus calculated as

$$673 \quad T_{(i,j,k+1)} = \frac{R_{(i,j,k)} - C q}{1 + mC}, \quad X_{(i,j,k+1)} = m T_{(i,j,k+1)} + q$$

674 **Equation A4**

675 where  $m$  and  $q$  are defined by the gradients and intercepts respectively, of the linear  
 676 sections of  $F$ .

677 Values of  $T$  and  $X$  on the boundaries of the modelled region of the crust are given by the  
 678 boundary conditions (Equations 3, 4 and 5) applied at  $x = \pm x_\infty$ . Because the solutions for  
 679  $T$  and  $X$  are generally symmetric about  $x = 0$ , the computational domain can be halved by  
 680 applying the boundary condition  $\frac{\delta T}{\delta x} = 0$ , at  $x = 0$  and restricting attention to the region  $0 \leq x \leq$   
 681  $x_\infty$ ,  $z_0 \leq z \leq z_l$ . Numerically, this condition can be applied using a quadratic interpolation of  $T$   
 682 near  $x = 0$ , leading to the result that

$$683 \quad T_{(0,k+1)} = \frac{1}{3} (4T_{(1,k+1)} - T_{(2,k+1)}).$$

684 **Equation A5**

685 Once the values of  $T_{(i,j,k+1)}$  are determined, Equation (9) can be used to determine  $T$  at the  
 686 dyke injection point ( $x = 0$ ).

### 687 **Analytical Solutions**

688 Various analytical results can be obtained for the 1D heat-flow equation, which can then be  
 689 used as approximations for the 2D heat-flow equation (Equation 1). The excess heat  
 690 content,  $Q$ , is independent of time and can be used to calculate the temperature at any given

691 time. This is because the excess heat content over all space  $-\infty < x < \infty$  at a general time  $\tau$   
692 must be equal to that of the dyke at  $\tau = 0$ . At large time  $\tau$ , the temperature can be found  
693 explicitly via  $x \sim 2 (\kappa\tau)^{1/2}$  (Turcotte and Schubert, 2002)

694 It is also possible to obtain an exact analytical solution to Equations (1) - (4) if the effect of  
695 latent heat is neglected ( $L=0$ ) (see, Carslaw and Jaeger 1950), which gives the peak  
696 temperature at the centre of the domain,  $x=0$ , in terms of error functions (see Daniels 2012  
697 for full details).

698

## 699 **Model Validation**

### 700 **1D Model**

701 The physical parameters were assigned values according to Table A.1. Initially, latent heat  
702 effects were ignored. This was done to test the model against the analytical solution that  
703 exists without  $L$  (Carslaw and Jaeger, 1950). Assuming the upper and lower surfaces ( $z_0$  and  
704  $z_1$  respectively) are sufficiently far apart, 1D analytical results are applicable to the 2D case  
705 for a fixed value of  $z$ . The decay over time of the dyke's thermal anomaly relative to the  
706 ambient temperature gives an analytical solution at large time  $\tau$  (Equation 4-170, Turcotte  
707 and Schubert 2002). An exact solution is obtained if the effect of latent heat is neglected  
708 ( $L=0$ , see, Carslaw and Jaeger 1950).

709 Figure A.1 A) shows the numerical solution for the peak temperature at the centre of the  
710 dyke,  $x = 0$ , as a function of time, along with the corresponding exact solution. There is  
711 excellent agreement, with the error reaching a maximum, yet small, value at small time  
712 where the numerical method has difficulty in accurately resolving the large change in  
713 temperature at the edge of the dyke (Figure A.1 B). Figure A.1 C) shows the heat content  
714 integral, per unit area of the dyke-country rock interface, plotted as a function of time. For  
715 these parameters (Table 4) it should have the constant value  $Q / \rho = 9.768 \times 10^6 \text{ J kg}^{-1} \text{ m}^{-1}$

716 and this is accurately reproduced for times  $\tau$  of up to about  $1.5 \times 10^9$  s. For larger times the  
717 outer boundaries of the computational domain begin to influence the solution because the  
718 diffusion scale  $x \sim 2 (\kappa\tau)^{1/2}$  becomes comparable with the size of the domain.

719 The effect of latent heat is now considered. The parameter values used are the same as  
720 those in Table 4 with latent heat  $L = 4 \times 10^5 \text{ J kg}^{-1}$  (Turcotte and Schubert 2002). Figures A.2  
721 A) and B) show the temperature profile obtained numerically at time  $\tau = 3.11 \times 10^9$  s for a  
722 dyke width of 5 m with  $\Delta\tau = 3600$  s,  $\Delta x = 1$  m and  $x_\infty = 200$  m, in excellent agreement with  
723 the analytical solutions. Figures A.2 C) and D) show the temperature at the centreline  $x = 0$   
724 as a function of time. A comparison is made with the analytical result where  $Q / \rho = 1.1768 \times$   
725  $10^7 \text{ J kg}^{-1} \text{ m}^{-1}$ . Figure A.2 E) and F) show that the numerical solution is consistent except for  
726 very small times where inaccuracy is introduced through the rapid change in temperature at  
727 the edge of the dyke.

728 Also, the 1D numerical model is tested against the analytical solution for the decay over time  
729 of the dyke thermal anomaly relative to the ambient temperature. At large time, the  
730 temperature at the centre of the numerical domain should decay as the square root of time:

731  $T(0, \tau) = \frac{Q}{2\rho C_p \sqrt{(\pi\kappa)}} \tau^{-1/2}$  (Equation 4.170, Turcotte and Schubert, 2002) Figure A.3 confirms

732 that this behaviour is accurately reproduced by the numerical solution.

733 Finally, tests were carried out to investigate the effect of step lengths  $\Delta x$  and  $\Delta\tau$  on the  
734 numerical solution. Figure A.4 A shows results obtained for the parameter values in Table 4,  
735  $L = 4 \times 10^5 \text{ J kg}^{-1}$  and a dyke width of 30 m. Computations were performed with  $x_\infty = 400$  m,  
736  $\Delta\tau = 3600$  s and three different spatial steps  $\Delta x = 2$  m, 6 m and 10 m. These confirm the  
737 gradual loss of accuracy with increasing  $\Delta x$ . Figure A.4 B shows results obtained for the  
738 same physical parameters but with a dyke width of 3 m. Here the computations were carried  
739 out with  $x_\infty = 100$  m,  $\Delta x = 1$  m and two different time steps  $\Delta\tau = 5000$  s and 10000 s. The  
740 reduction in accuracy by using the larger time step is not significant and justifies the use of a

741 larger time step in subsequent calculations, provided the condition for numerical stability is  
742 maintained.

### 743 **One-dimensional versus two-dimensional models**

744 The boundary effect at the top and bottom of the 2D model gradually has an effect on larger  
745 and larger areas of the interior solution with increasing time. At the top of the computational  
746 domain, this is analogous to the surface cooling of the system and allows an appreciation of  
747 the likely effect of surface cooling on the system after any specified time (Figure A.5). Except  
748 at the top and bottom of the two-dimensional model, the one and two-dimensional models  
749 yield same solutions. This is shown in Figure A.6 where the two-dimensional solution at  
750 different depths ( $z$ ) has been compared with a one-dimensional model solution for that  
751 depth. The interior solutions to the 2D numerical model are comparable with the 1D model  
752 results.

753

### 754 **Figure captions**

755 Figure A.1: Comparison of the 1D numerical solution for  $L=0$  J/kg,  $T_m = 1320^\circ\text{C}$  and  $\omega = 2.5$   
756 m with the analytical solution for the peak temperature over time. A) The numerical and  
757 analytical peak temperatures. B) The difference between the analytically and numerically  
758 calculated temperature values. The difference is calculated as the analytical temperature  
759 minus the numerical temperature. C) Heat content integral as a function of time for the  
760 computation of A) and B). D) The percentage difference between the calculated heat content  
761 integral and the expected analytical value.

762 Figure A.2: A) 1D numerical solution for  $L = 4 \times 10^5$  J/kg,  $T_m = 1320^\circ\text{C}$  and  $\omega = 2.5$  m at time  
763  $= 3.11 \times 10^9$  s (100 years) using  $\Delta\tau = 3600$  s and  $\Delta x = 1$  m; the large-time analytical solution  
764 is also shown. B) The difference between the analytical and numerical solutions. C) 1D  
765 numerical solution for the peak temperature at the centreline  $x = 0$  as a function of time for



766 the computation of A) and B); the large-time analytical solution is also shown. D) The  
767 difference between the analytical and numerical solutions. E) Heat content (Q) as a function  
768 of time for the computation of A) and B). F) The percentage difference between the  
769 calculated heat content integral and the expected analytical value.

770 Figure A.3: The ratio of the 1D numerical solution to the exact analytical solution for the  
771 temperature at the centre of the dyke  $\frac{T(0,\tau) \sqrt{2\rho C_p(\pi\kappa)^{\frac{1}{2}}}}{Q}$ , as a function of time for the  
772 computation of Figure A.2. Close proximity to the analytical solution is achieved almost  
773 immediately with the exact analytical solution reached in 30.95 years or 315 time steps.

774 Figure A.4: A) Difference between the analytical and numerical solutions for  $L = 4 \times 10^5$  J/kg,  
775  $T_m = 1320^\circ\text{C}$  and  $\omega = 15$  m at time  $\tau = 3.11 \times 10^9$  s (100 years) using  $\Delta\tau = 3600$  s and  $\Delta x = 2$   
776 m, 6 m, and 10 m. B) Difference between the analytical and numerical solutions for  $L = 4 \times$   
777  $10^5$  J/kg,  $T_m = 1320^\circ\text{C}$  and  $\omega = 1.5$  m at time  $\tau = 10^8$  s (1157 days /  $\sim 3.2$  years) using  $\Delta x =$   
778 1 m with  $\Delta\tau = 5000$  s and 10000 s.

779 Figure A.5: Temperature contours for the numerical computations of the 2D heat-flow  
780 equation with  $L = 4 \times 10^5$  J/kg,  $T_m = 1320^\circ\text{C}$ ,  $z_0 = 1000$  m,  $z_1 = 5000$  m,  $Q_0/K = 0.03^\circ\text{C/m}$  and  
781  $\omega = 7.5$  m, obtained using  $x_\infty = 4000$  m,  $\Delta x = \Delta z = 5$  m,  $\Delta\tau = 3.11 \times 10^6$  s. The temperature  
782 shown is that recorded at the time step immediately prior to the next injection at time =  $2.49$   
783  $\times 10^{12}$  s (80 ka) for extension rate  $S = 25$  mm/yr.

784 Figure A.6: Numerical solutions for the 2D model with  $L = 4 \times 10^5$  J/kg,  $T_m = 1320^\circ\text{C}$ ,  $z_0 =$   
785 1000 m,  $z_1 = 5000$  m,  $Q_0/K = 0.03^\circ\text{C/m}$  and  $\omega = 7.5$  m with an extension rate  $S = 25$  mm/yr;  
786 also the equivalent 1D calculations at depths  $z$  given by A) 1500 m, B) 2750 m, C) 3000 m,  
787 D) 3250 m, E) 4500 m obtained using  $z(Q_0/K)$ . The computations were performed with  $x_\infty =$   
788 4000 m,  $\Delta x = \Delta z = 5$  m,  $\Delta\tau = 3.11 \times 10^6$  s and show the temperature recorded immediately  
789 prior to the next injection at time =  $6.22 \times 10^{11}$  s ( $\sim 20$  ka).

790

791 **Table caption**

792 Table A.1: The initial parameter values used to test the 1D model against the analytical  
793 solution. <sup>a</sup>Annen and Sparks (2002); Bohrson and Spera (2001); Laube and Springer (1998);  
794 Rivers and Carmichael (1987). <sup>b</sup>Using  $\kappa = K / \rho C_p$ , with  $K = 1.15 \text{ W/m/K}$  (Spera, 2000),  $\rho =$   
795  $2.8 \times 10^3 \text{ kg/m}^3$  (Annen and Sparks, 2002) and  $C_p = 1.48 \times 10^3 \text{ J/kg}$  (Annen and Sparks,  
796 2002)

**Highlights**

- A numerical solution to the heat-flow equation is developed
- Dyking has a significant thermal effect on crust rheology during rifting
- Extension rate exerts first-order control on crustal thermal structure during rifting
- The crust is expected to heat considerably on time-scales of less than 1 Ma
- In the MER dyking has localised for insufficient time for significant crustal heating

Figure1\_Daniels

[Click here to download Figure: FIGURE\\_1\\_Daniels.pdf](#)

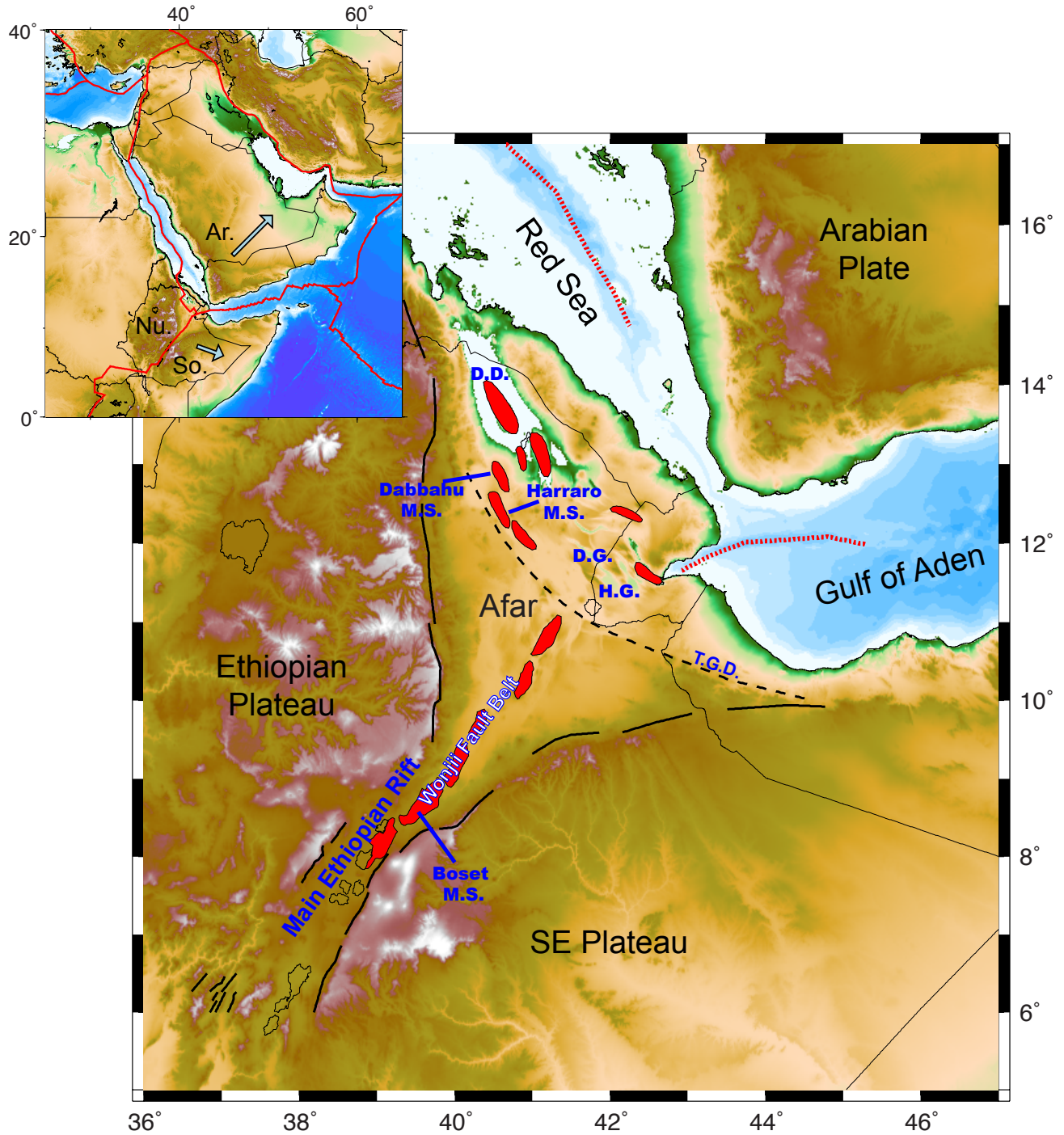


Figure 2 Daniels

[Click here to download Figure: FIGURE\\_2\\_Daniels.pdf](#)

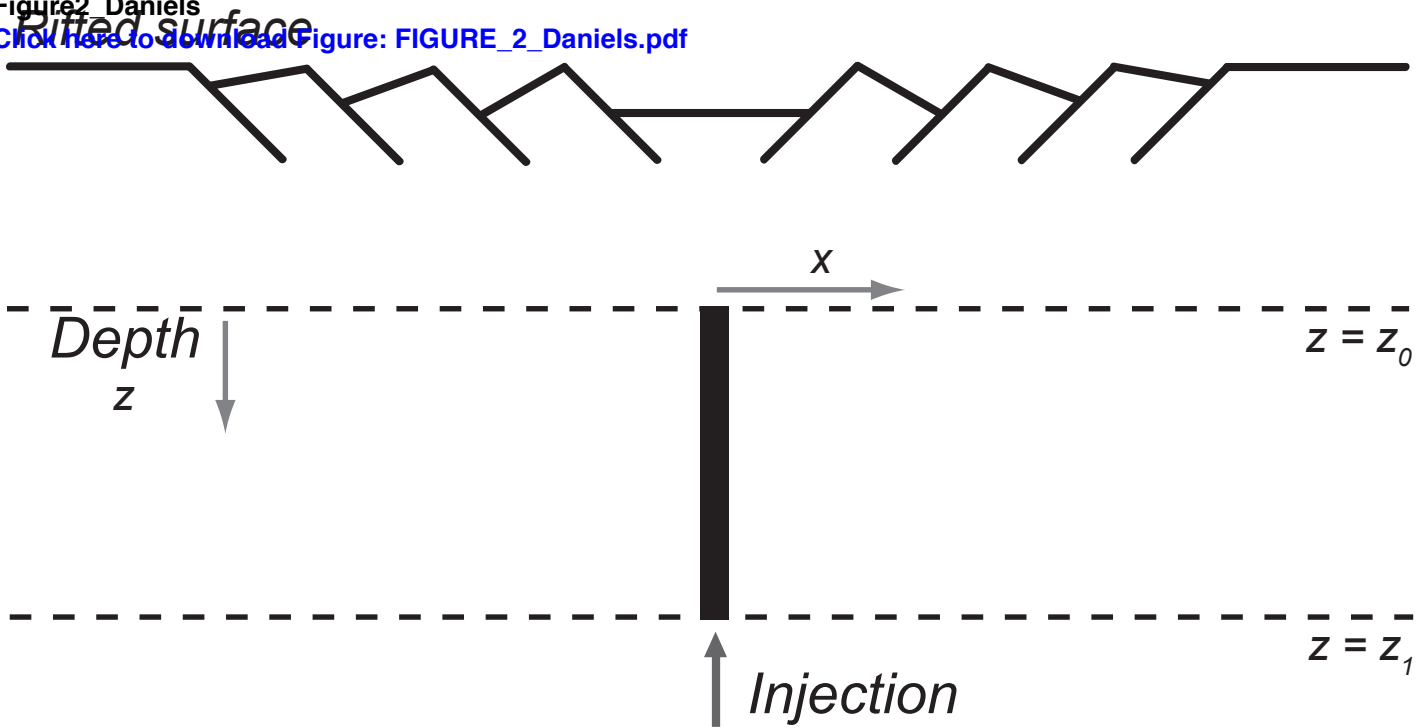


Figure3\_Daniels

[Click here to download Figure: FIGURE\\_3\\_NEW\\_Daniels.pdf](#)

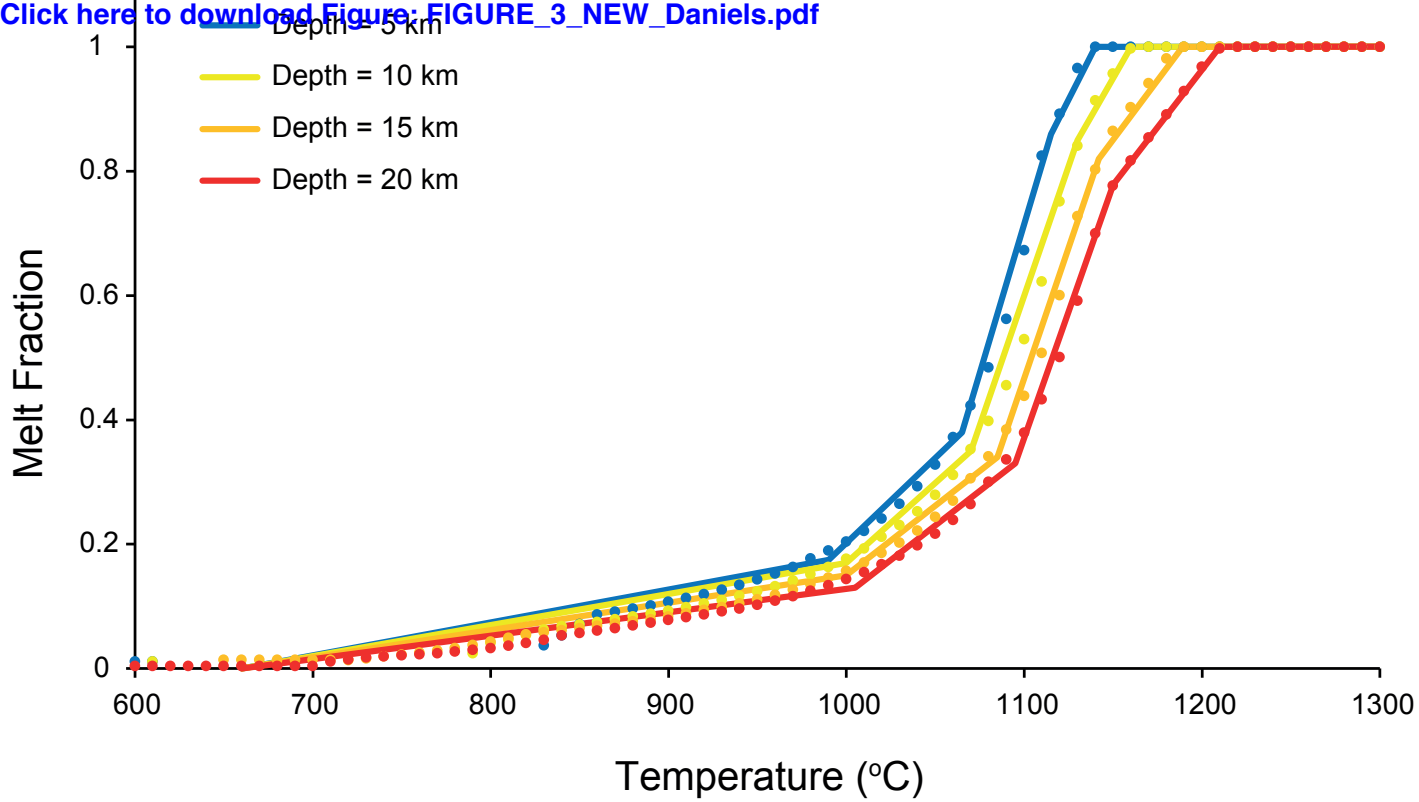
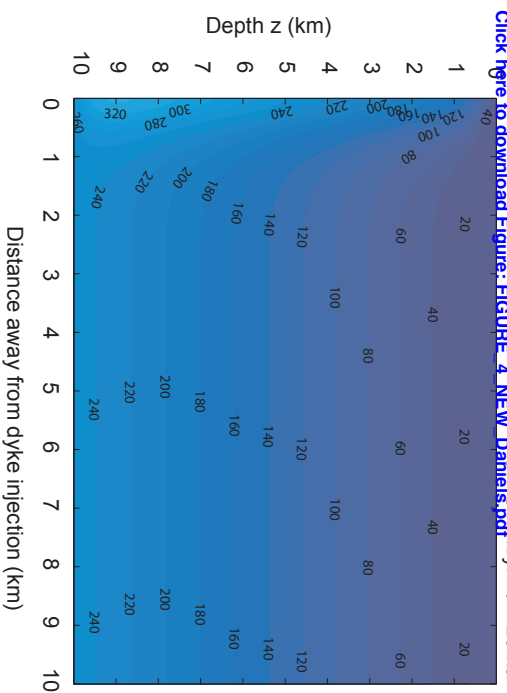
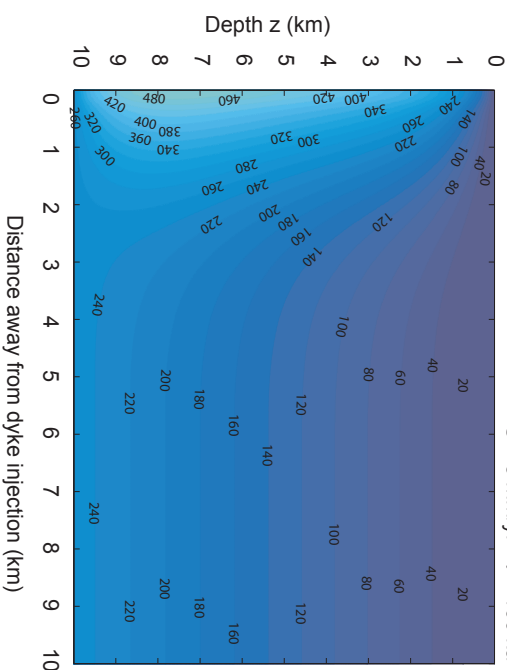


Figure 4. Daniels

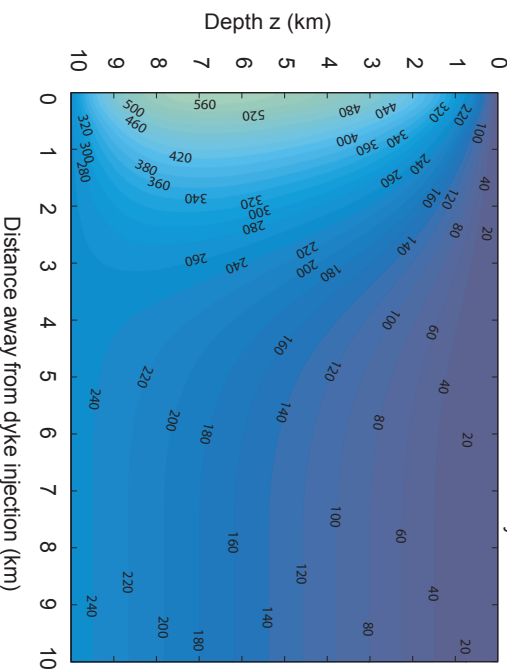
$S = 5 \text{ mm/yr}$   $\tau = 20 \text{ ka}$



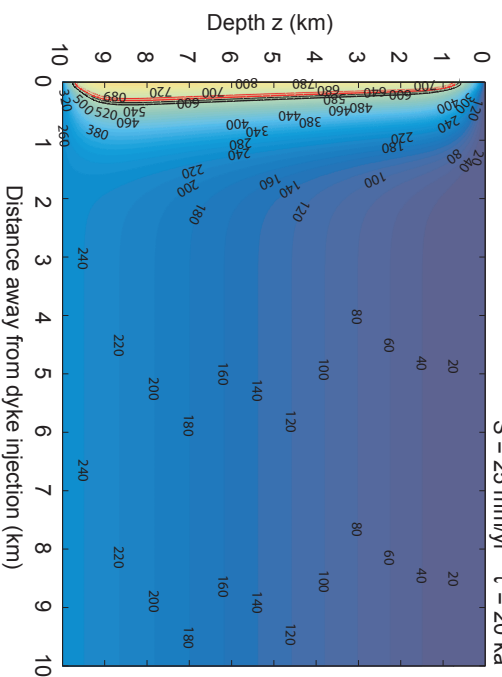
$S = 5 \text{ mm/yr}$   $\tau = 100 \text{ ka}$



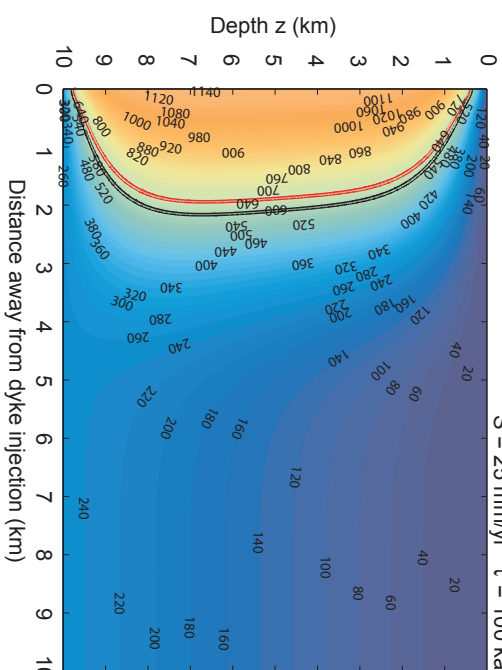
$S = 5 \text{ mm/yr}$   $\tau = 200 \text{ ka}$



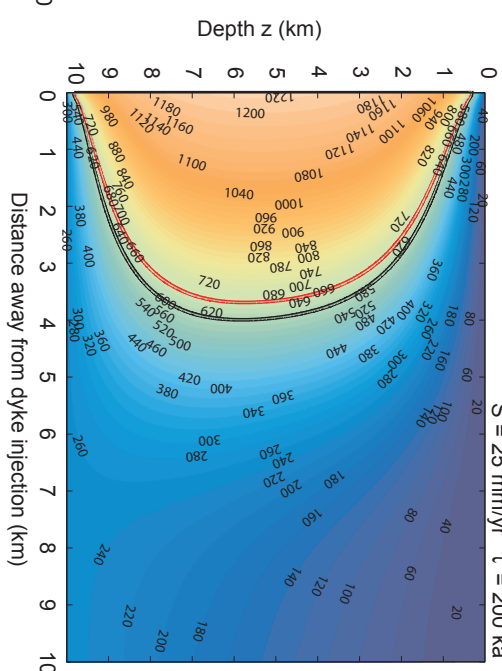
$S = 25 \text{ mm/yr}$   $\tau = 20 \text{ ka}$



$S = 25 \text{ mm/yr}$   $\tau = 100 \text{ ka}$



$S = 25 \text{ mm/yr}$   $\tau = 200 \text{ ka}$



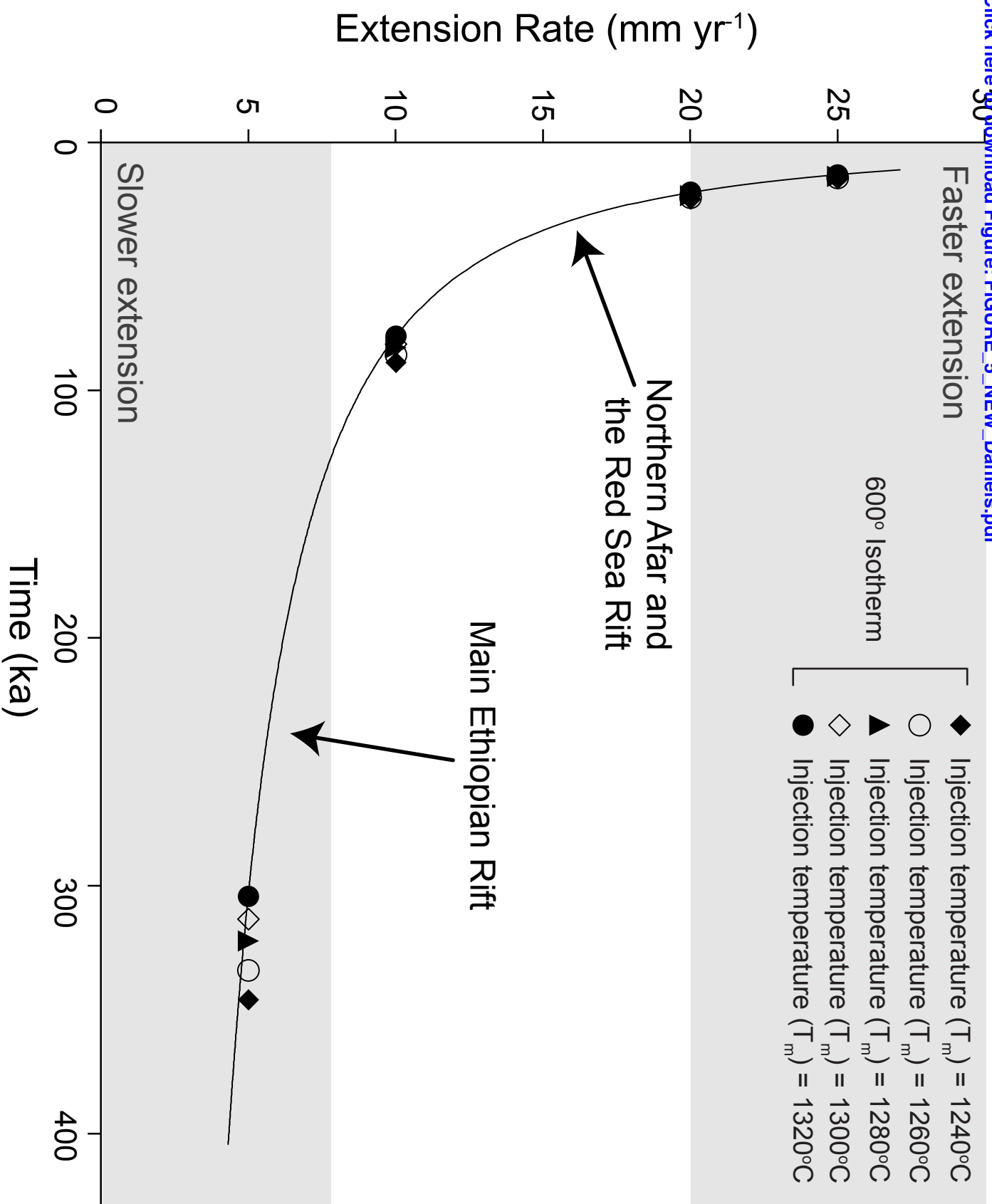
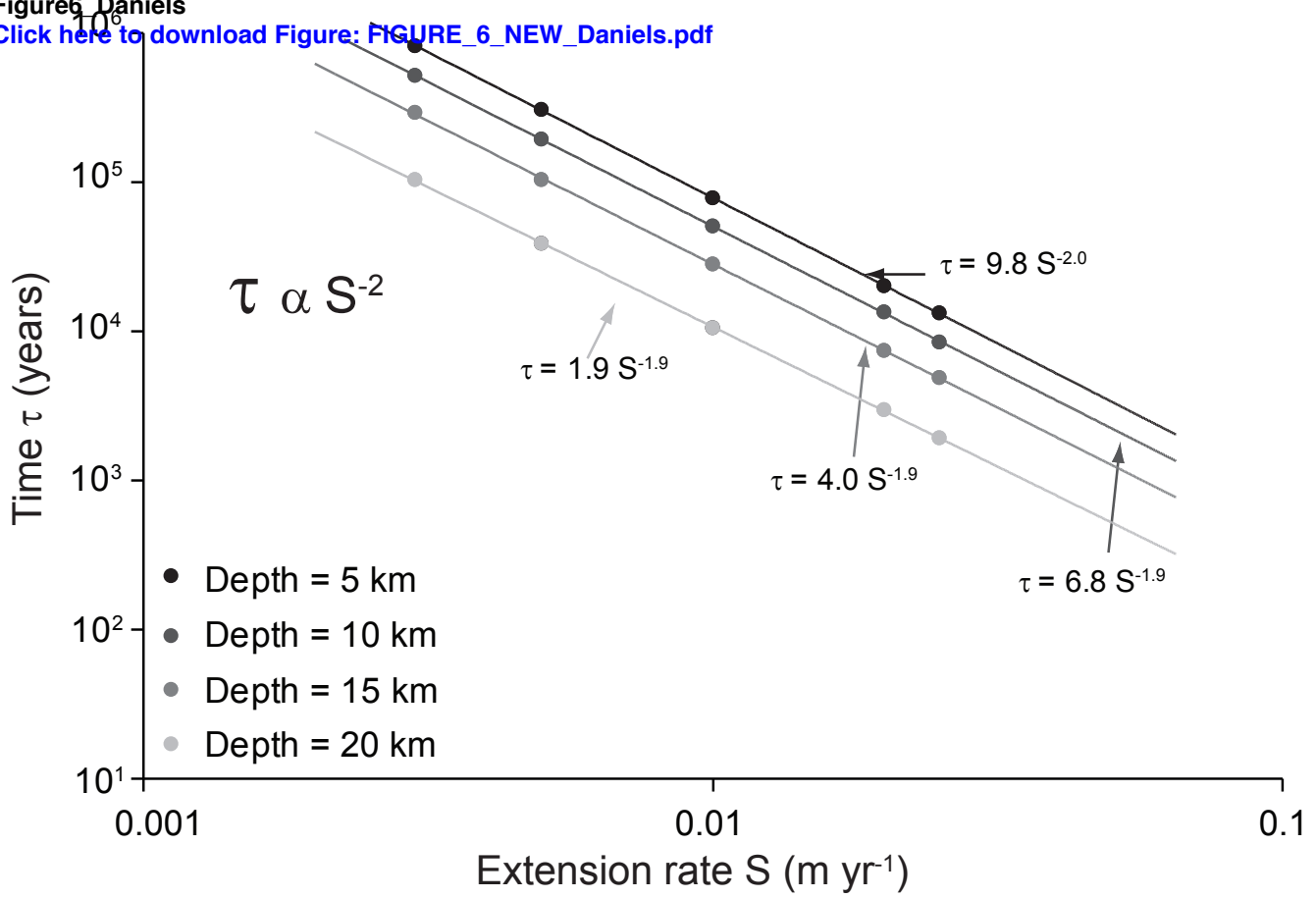
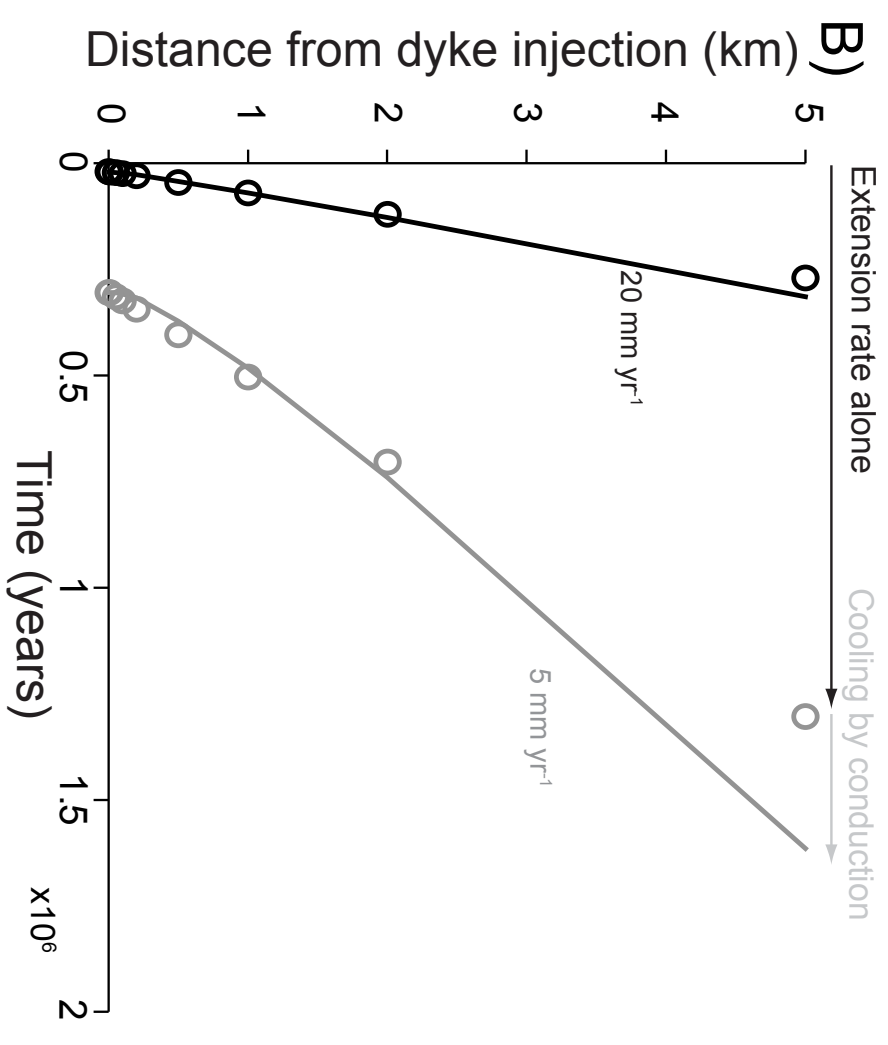
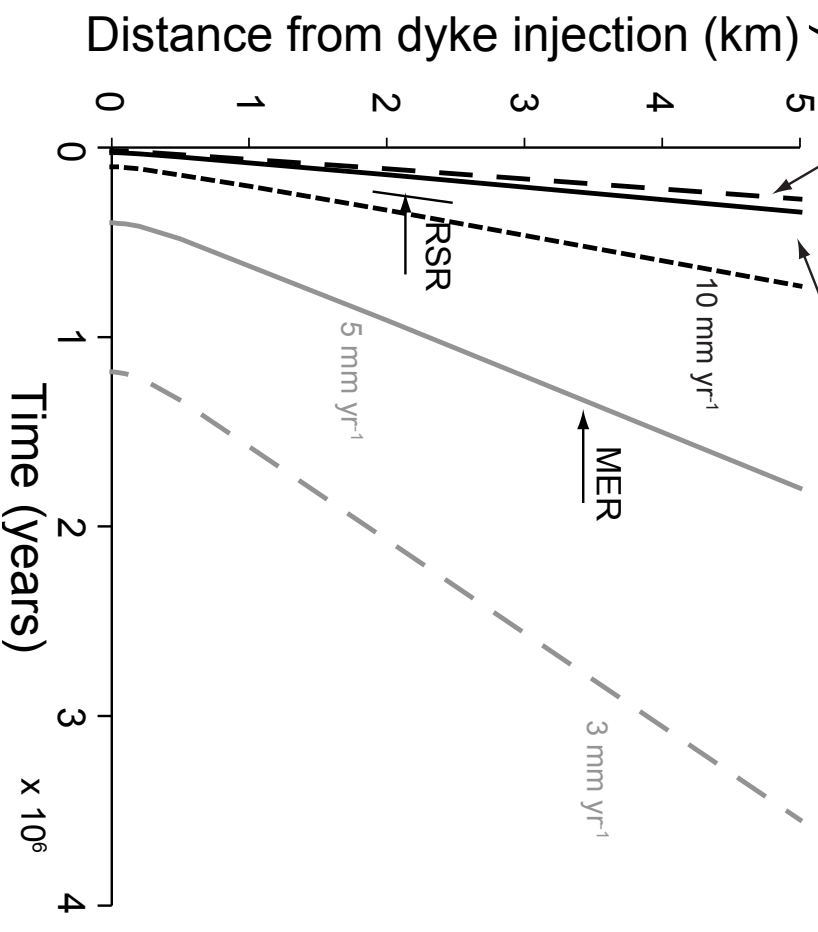




Figure 6 Daniels

[Click here to download Figure: FIGURE\\_6\\_NEW\\_Daniels.pdf](#)





**Table1\_Daniels**[Click here to download Table: Table1\\_NEW\\_Daniels.xlsx](#)

Pressure	1373.4	2746.8	4120.4	5493.6
$T_l$	1140	1160	1189	1210
$X_l$	1	1	1	1
$T_c$	1115	1130	1142	1150
$X_c$	0.860	0.850	0.820	0.778
$T_{c2}$	1065	1070	1085	1095
$X_{c2}$	0.380	0.350	0.340	0.330
$T_e$	990	1000	1000	1005
$X_e$	0.175	0.170	0.150	0.130
$T_s$	660	660	660	660
$X_s$	0	0	0	0

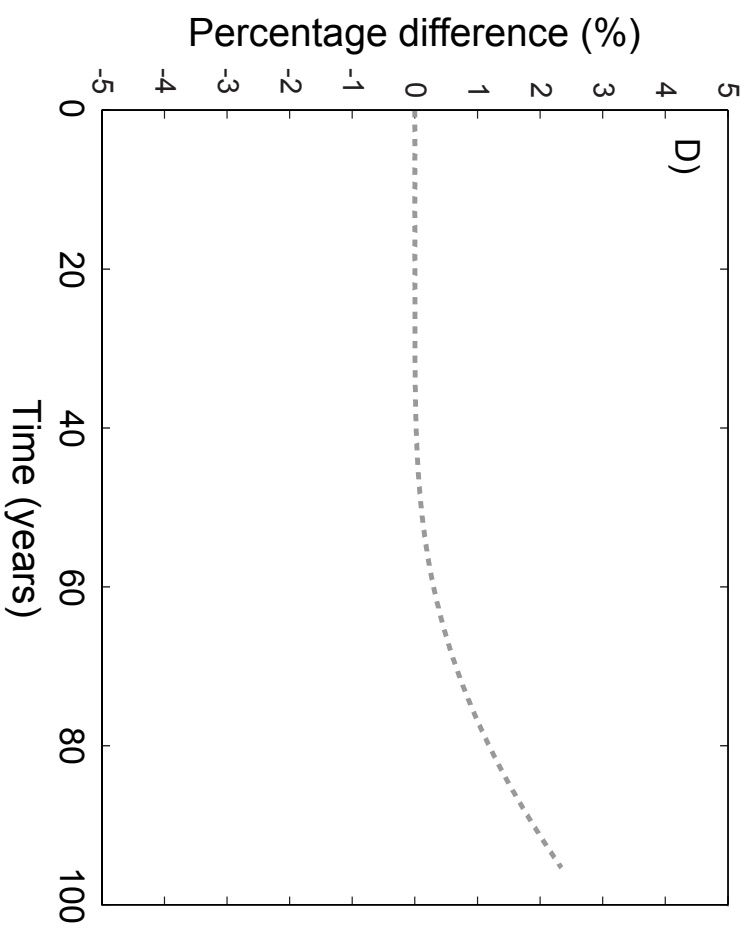
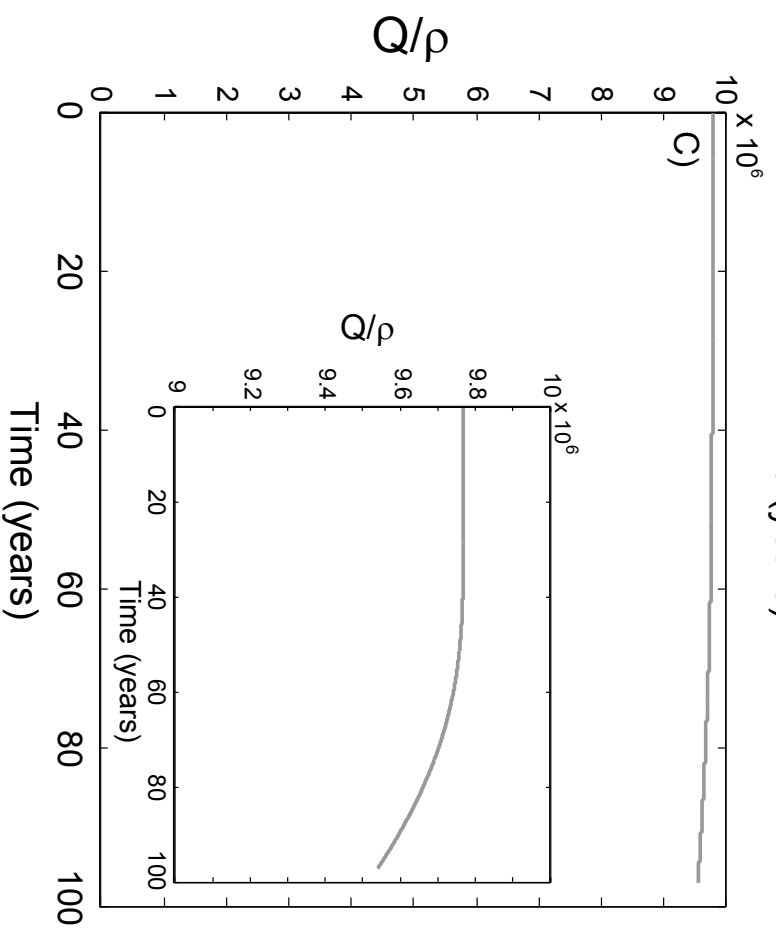
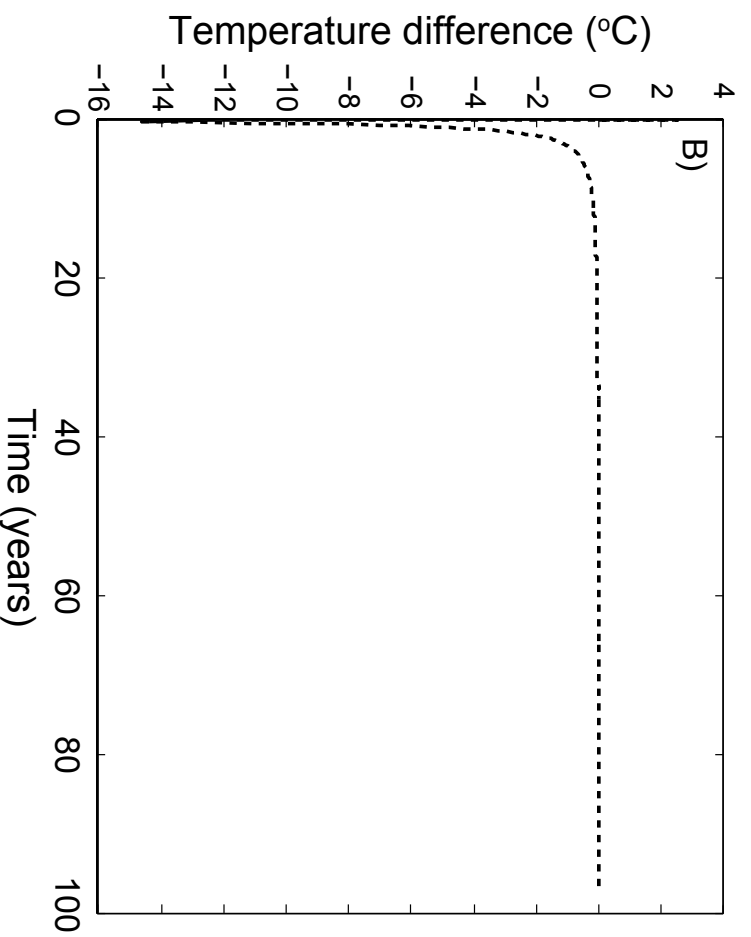
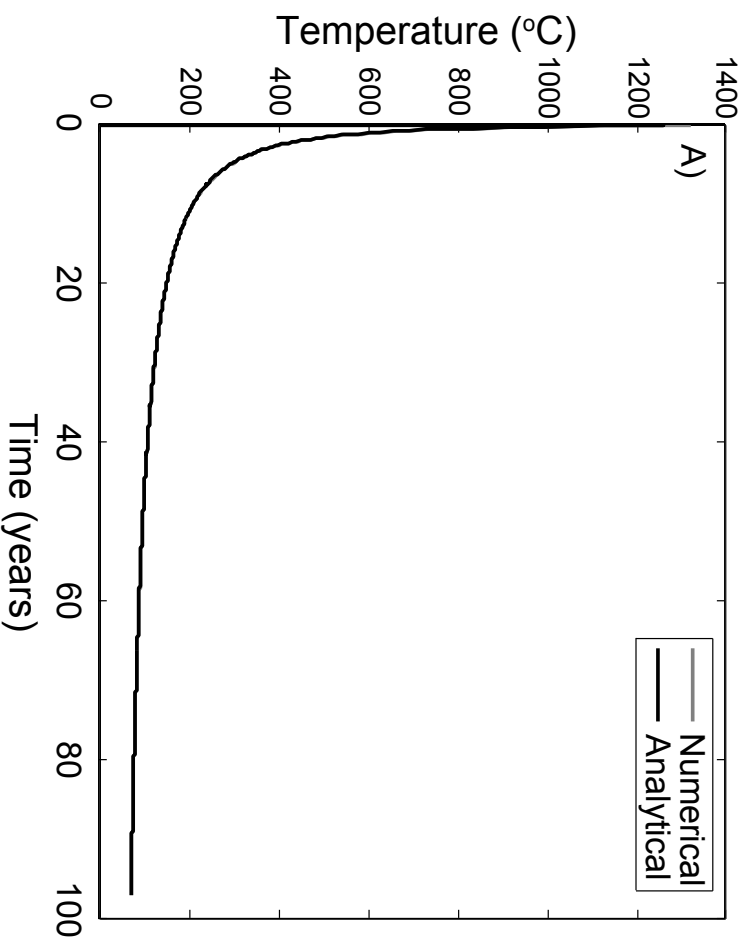
**Table2\_Daniels**[Click here to download Table: Table2\\_NEW\\_Daniels3.xlsx](#)

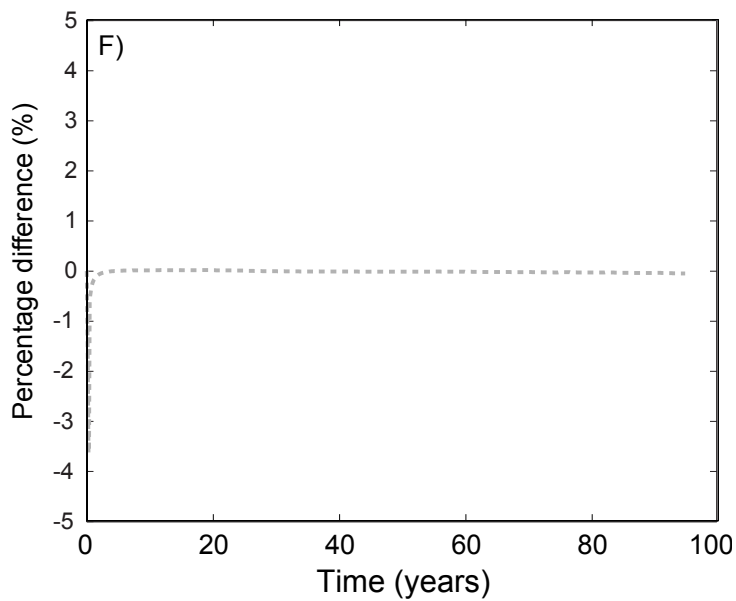
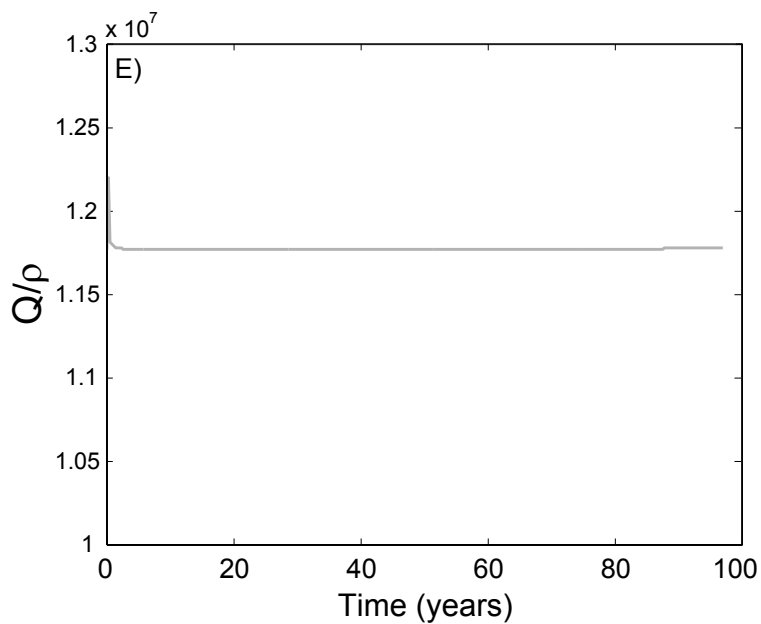
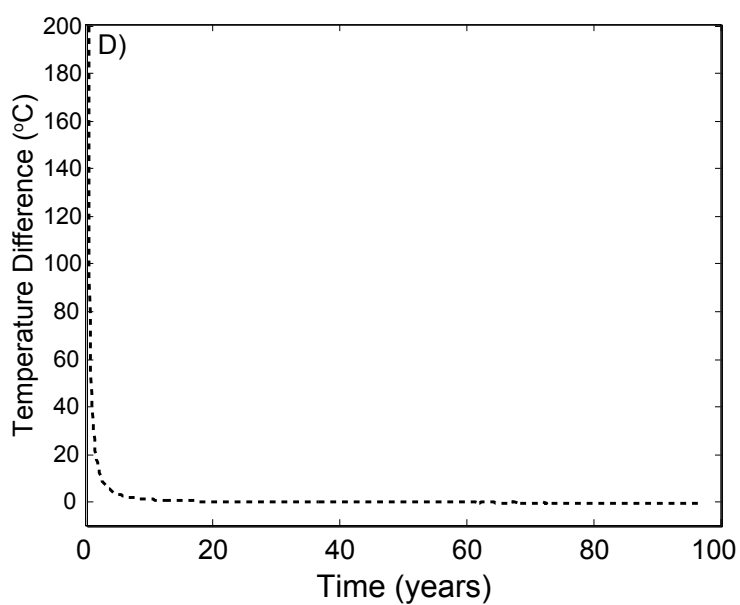
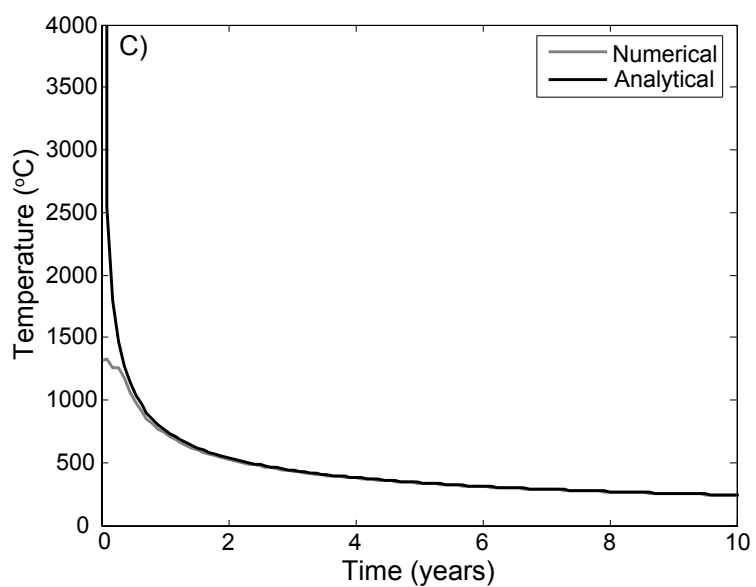
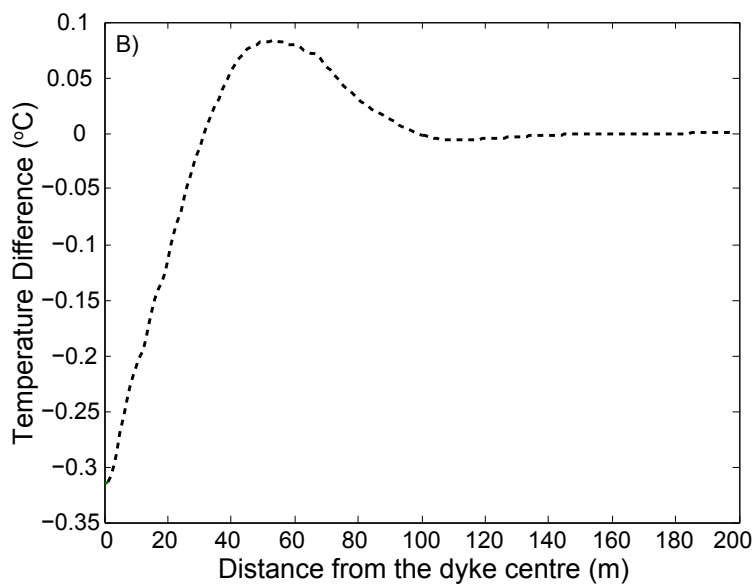
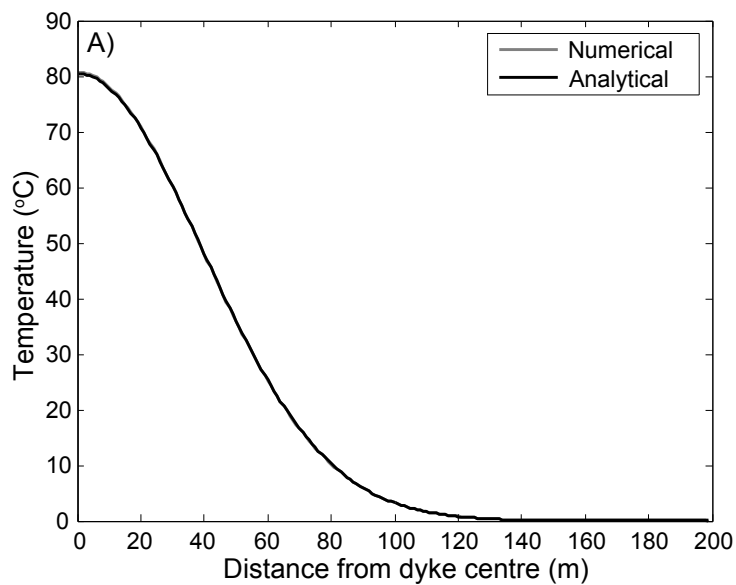
Parameter		Values	Units
$\Delta x, \Delta z$	Array cell size	5	m
$\Delta t$	Timestep size	3110400	s
$\omega$	Dyke half thickness	15	m
$\rho$	Density <sup>a</sup>	2800	kg / m <sup>3</sup>
$k$	Thermal conductivity <sup>b</sup>	2.2	W / m / K
$\kappa$	Thermal diffusivity	$5.3 \times 10^{-7}$	m <sup>2</sup> / s
$L$	Specific latent heat <sup>a</sup>	$4 \times 10^5$	J / kg / K
$C_p$	Specific heat capacity <sup>a</sup>	1480	J / kg
$Q_o$	Surface heat flux <sup>c</sup>	60	mW / m <sup>2</sup>
$A$	Heat production <sup>c</sup>	$8 \times 10^{-7}$	W/m <sup>3</sup>

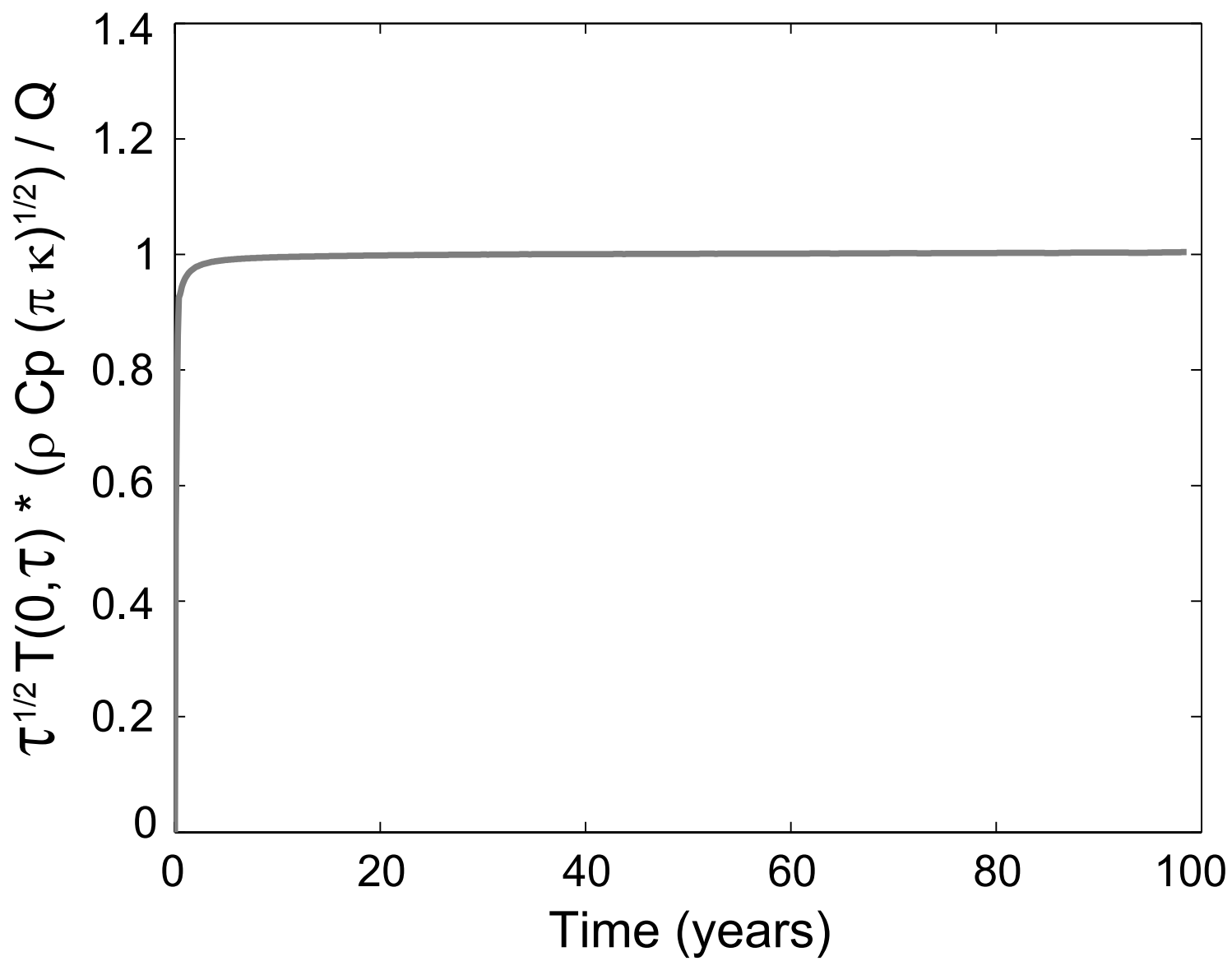
Table3\_Daniels

[Click here to download Table: Table3\\_NEW\\_Daniels.xlsx](#)

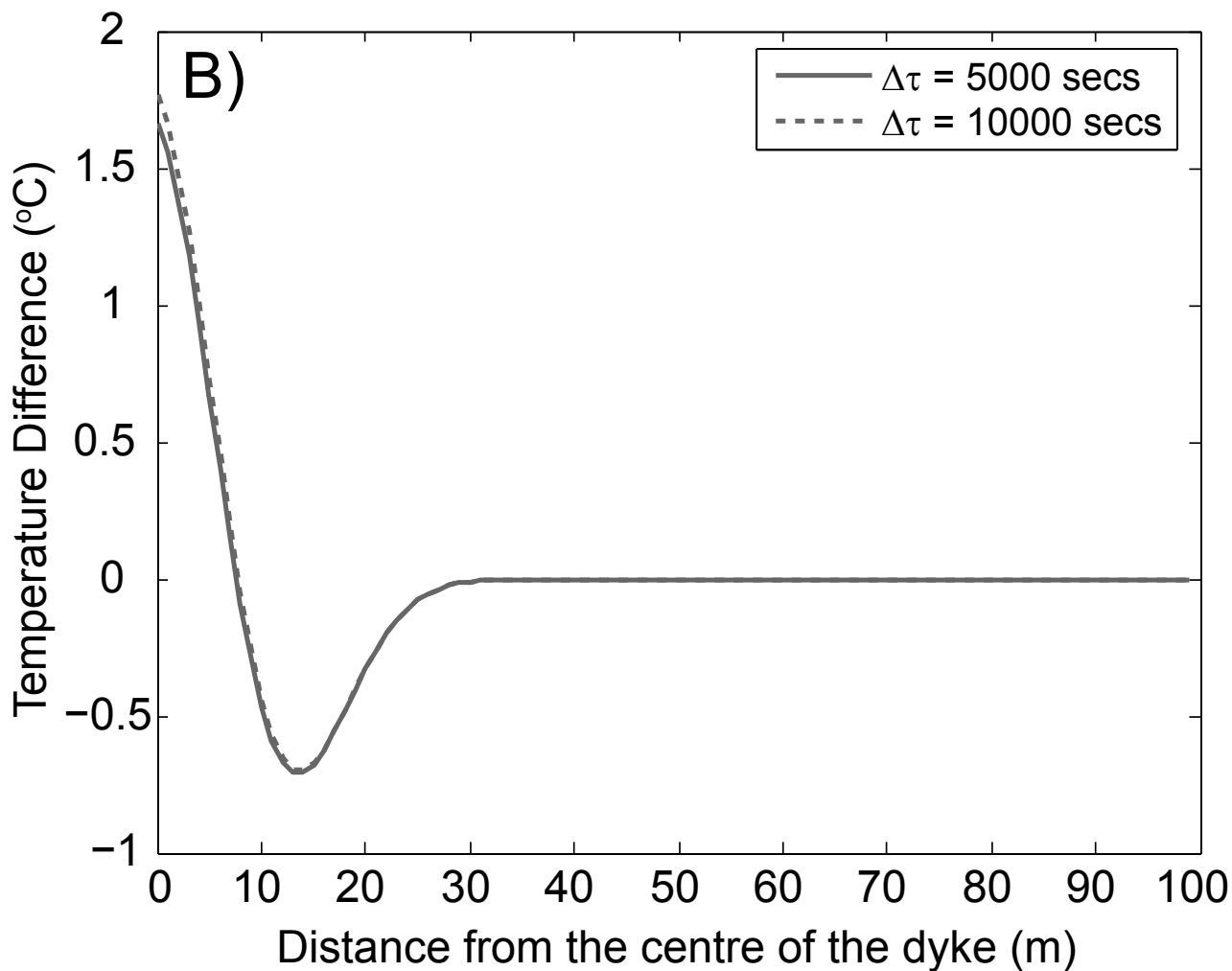
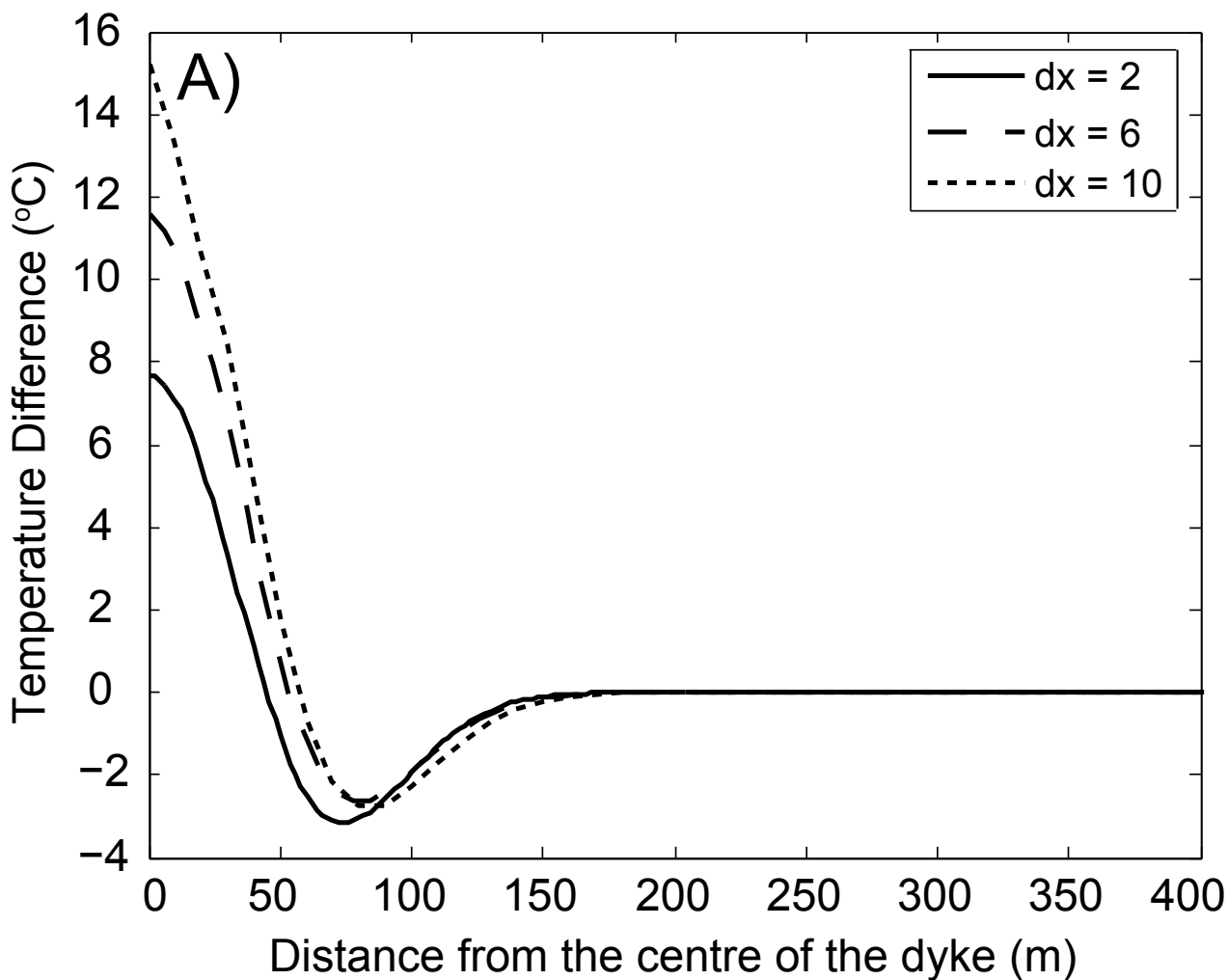
Depth (km)		5	10	15	20
Extension rate (mm / yr)					
Solidus	3	$1.18 \times 10^6$	$8.18 \times 10^5$	$4.63 \times 10^5$	$2.17 \times 10^5$
	5	$3.96 \times 10^5$	$2.66 \times 10^5$	$1.66 \times 10^5$	$8.29 \times 10^4$
	10	$1.01 \times 10^5$	$6.96 \times 10^4$	$4.30 \times 10^4$	$2.23 \times 10^4$
	20	$2.60 \times 10^4$	$1.79 \times 10^4$	$1.12 \times 10^4$	$6.06 \times 10^3$
	25	$1.67 \times 10^4$	$1.14 \times 10^4$	$7.24 \times 10^3$	$3.70 \times 10^3$
600°C Isotherm	3	$8.18 \times 10^5$	$5.18 \times 10^5$	$2.91 \times 10^5$	$1.04 \times 10^5$
	5	$3.04 \times 10^5$	$1.92 \times 10^5$	$1.04 \times 10^5$	$3.86 \times 10^4$
	10	$7.82 \times 10^4$	$5.04 \times 10^4$	$2.81 \times 10^4$	$1.05 \times 10^4$
	20	$2.01 \times 10^4$	$1.35 \times 10^4$	$7.39 \times 10^3$	$2.96 \times 10^3$
	25	$1.32 \times 10^4$	$8.43 \times 10^3$	$4.88 \times 10^3$	$1.92 \times 10^3$

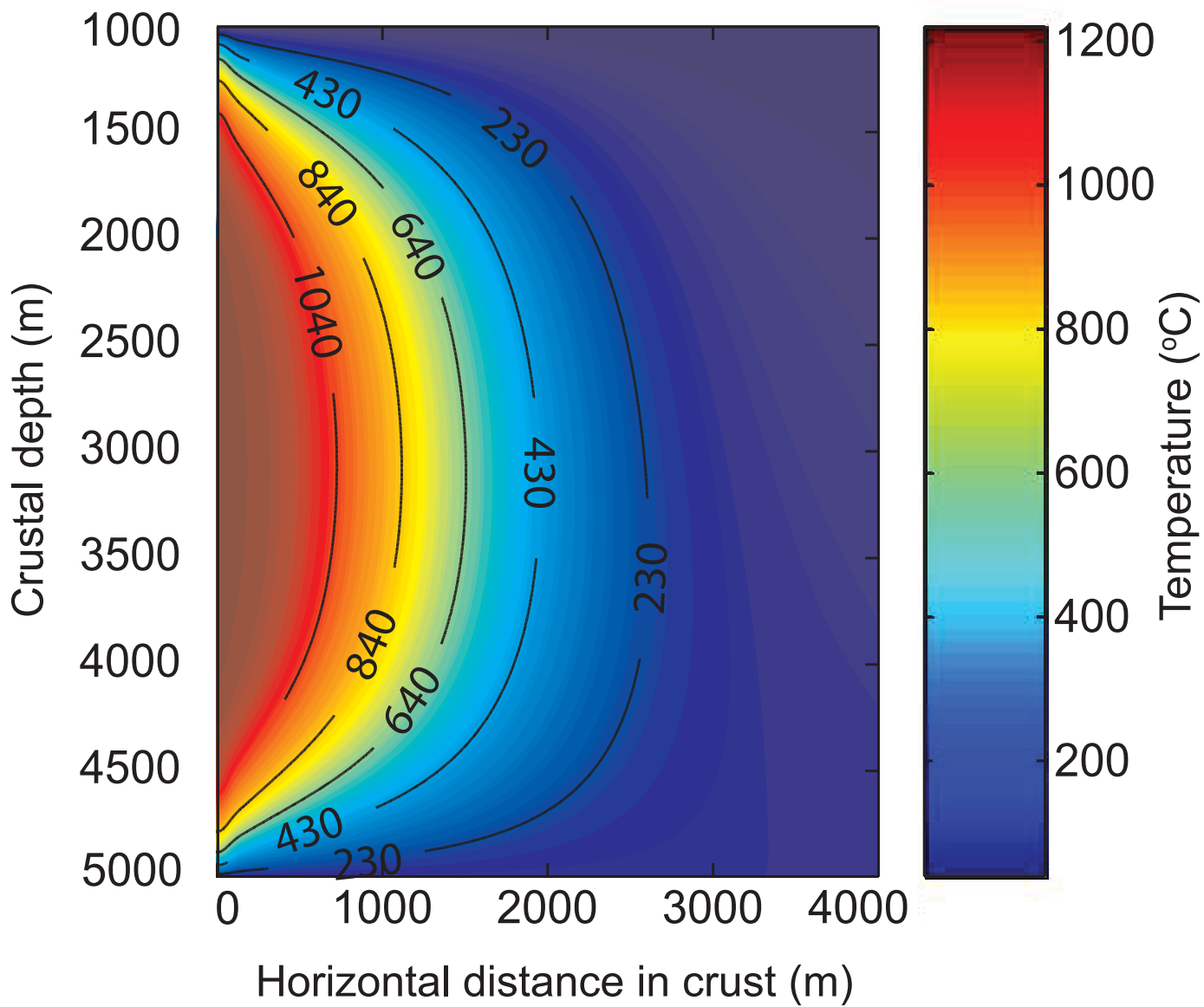


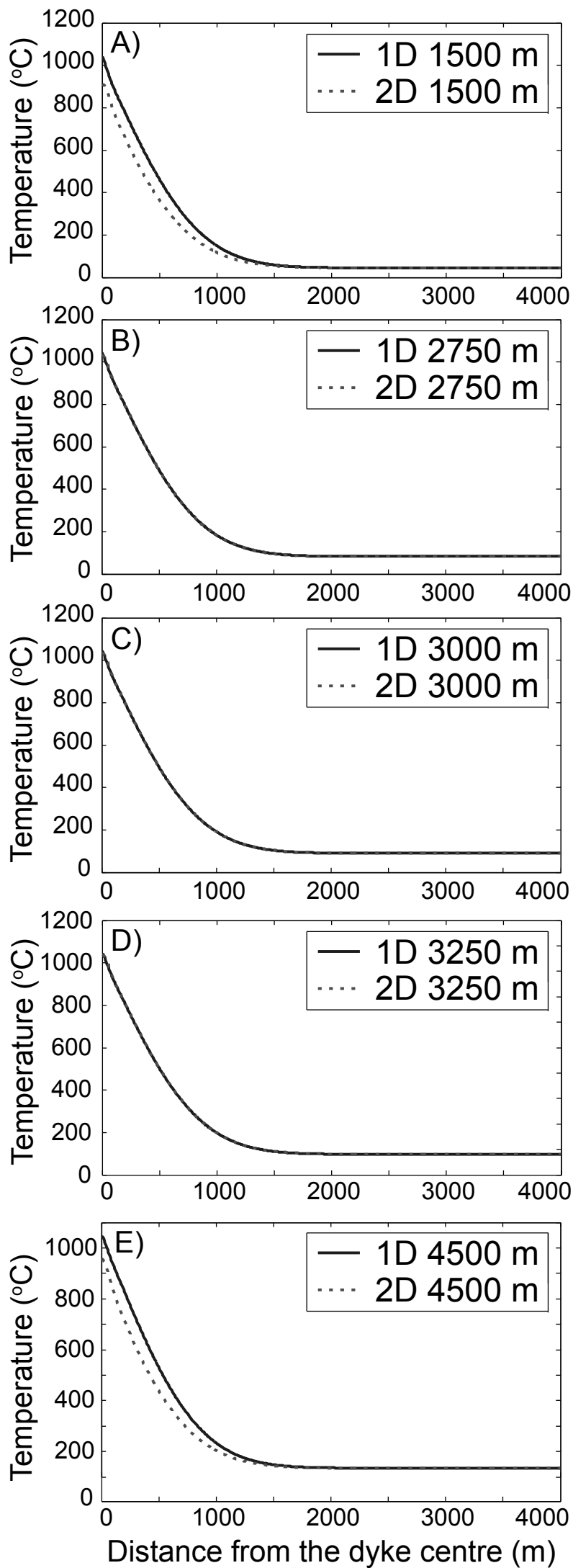












Parameter		Values	Units
$T_0$	Initial temperature	0	$^{\circ}\text{C}$
$T_m$	Magma temperature	1320	$^{\circ}\text{C}$
$\omega$	Dyke half thickness	2.5	m
$x_{\infty}$	Computational domain	100	m
L	Specific latent heat	$4 \times 10^5$	J / kg
$C_p$	Specific heat capacity <sup>a</sup>	1480	J / kg / K
$\kappa$	Thermal diffusivity <sup>b</sup>	$2.5 \times 10^{-7}$	$\text{m}^2 / \text{s}$